INTERFACE PASSIVATION OF PEROVSKITE SOLAR CELLS WITH NOVEL CATIONS

A THESIS SUBMITTED TO
THE GRADUATE SCHOOL OF NATURAL AND APPLIED SCIENCES
OF
MIDDLE EAST TECHNICAL UNIVERSITY

BY

GÜLSEVİM BENSU ÇEL

IN PARTIAL FULFILLMENT OF THE REQUIREMENTS
FOR
THE DEGREE OF MASTER OF SCIENCE
IN
MICRO AND NANOTECHNOLOGY

AUGUST 2022

Approval of the thesis:

INTERFACE PASSIVATION OF PEROVSKITE SOLAR CELLS WITH NOVEL CATIONS

submitted by **GÜLSEVİM BENSU ÇEL** in partial fulfillment of the requirements for the degree of **Master of Science** in **Micro and Nanotechnology, Middle East Technical University** by,

Prof. Dr. Halil Kalıpçılar
Dean, Graduate School of **Natural and Applied Sciences** _____

Prof. Dr. Deniz Üner
Head of the Department, **Micro and Nanotechnology** _____

Assoc. Prof. Dr. E. Görkem Günbaş
Supervisor, **Micro and Nanotechnology, METU** _____

Assoc. Prof. Dr. Selçuk Yerci
Co-Supervisor, **Electric-Electronics Engineering, METU** _____

Examining Committee Members:

Prof. Dr. Serap Güneş
Physics, Yıldız Teknik University _____

Assoc. Prof. Dr. E. Görkem Günbaş
Micro and Nanotechnology, METU _____

Assoc. Prof. Dr. Selçuk Yerci
Electric-Electronics Engineering, METU _____

Assist. Prof. Dr. Yusuf Keleştemur
Metallurgical and Materials Engineering, METU _____

Assoc. Prof. Dr. Kuroş Salimi
Chemical Engineering, Ankara Yıldırım Beyazıt University _____

Date: 19.08.2022

I hereby declare that all information in this document has been obtained and presented in accordance with academic rules and ethical conduct. I also declare that, as required by these rules and conduct, I have fully cited and referenced all material and results that are not original to this work.

Name Last name : Çel, Gülsevim Bensu

Signature :

ABSTRACT

INTERFACE PASSIVATION OF PEROVSKITE SOLAR CELLS WITH NOVEL CATIONS

Çel, Gülsevim Bensu
Master of Science, Micro and Nanotechnology
Supervisor: Assoc. Prof. Dr. E. Görkem Günbaş
Co-Supervisor: Assoc. Prof. Dr. Selçuk Yerci

August 2022, 75 pages

Interface engineering and surface defect passivation play an important role in the development of state-of-the-art perovskite solar cells. Forming an additional two-dimensional (2D) layer on top of the primary perovskite absorber after treatment with organic spacers not only passivates defects and improves the device performance, but also enhances stability. In this study, two novel cations, that are 2,6-methoxy-phenylethyl ammonium iodide (2,6-MeO-PEAI) and 3,5-methoxy-phenylethyl ammonium iodide (3,5-MeO-PEAI) were used on top of $(FAPbI_3)_{1-x}(MAPbBr_3)_x$ (FAMA) perovskite, which resulted in an increase in open-circuit voltage (V_{OC}) and enhancement of stability. Additionally, the effect of annealing after cation treatment was investigated in detail. Grazing incidence X-ray diffraction measurements revealed that 2,6-MeO-PEAI salt did not form pure 2D perovskite, whereas 3,5-MeO-PEAI salt created a 2D layer upon annealing. Both photoluminescence and impedance spectroscopy measurements indicated that nonradiative recombination was reduced upon salt treatment, which led to an increase in V_{OC}. A V_{OC} value as high as 1.14 eV was achieved with the addition of

3,5-MeO-PEAI salt, however, cells with 2,6-MeO-PEAI salt exhibited the best overall performance, exceeding the efficiency of reference cells. The power conversion efficiency (PCE) increased from 18.14% for the reference cell to 19.15% for the cell treated with 2,6-MeO-PEAI. Moreover, moisture resistance of the salt-treated devices enhanced greatly, which was proved with contact angle measurements. After six weeks from the fabrication, the reference cell, and the cells treated with 2,6-MeO-PEAI and 3,5-MeO-PEAI maintained 77%, 93% and 94% of the initial PCE, respectively, which clearly demonstrated the long-term stability enhancement upon salt treatment.

Keywords: Perovskite Solar Cell, 3D/2D Perovskite, Interface Passivation, Organic Spacer Cations

ÖZ

ÖZGÜN KATYONLAR İLE PEROVSKİT GÜNEŞ HÜCRELERİNİN YÜZEY PASİVASYONU

Çel, Gülsevim Bensu
Yüksek Lisans, Mikro ve Nanoteknoloji
Tez Yöneticisi: Doç. Dr. E. Görkem Günbaş
Ortak Tez Yöneticisi: Doç. Dr. Selçuk Yerci

Ağustos 2022, 75 sayfa

Arayüz mühendisliği ve yüzey kusurlu pasifleştirme, son teknoloji ürünü perovskite güneş pillerinin geliştirilmesinde önemli bir rol oynamaktadır. Organik aralayıcılar ile birincil perovskit soğurucunun üstünde iki boyutlu (2D) katman oluşturmak, yalnızca tane sınırlarını pasifleştirmekle ve cihaz performansını iyileştirmekle kalmaz, aynı zamanda stabiliteyi de artırır. Bu çalışmada 2,6-metoksi-feniletil amonyum iyodür (2,6-MeO-PEAI) ve 3,5-metoksi-feniletil amonyum iyodür (3,5-MeO-PEAI) olmak üzere iki yeni katyon $(FAPbI_3)_{1-x}(MAPbBr_3)_x$ (FAMA) perovskitinin üstünde kullanılmıştır, bu da açık devre voltajında (V_{OC}) bir artışa ve stabilitenin artmasına neden olmuştur. Ayrıca katyon pasivasyonu sonrası tavlamanın etkisi detaylı olarak incelenmiştir. Otlatma insidansı X-ışını kırınımı ölçümleri, 2,6-MeO-PEAI tuzunun 2D perovskit oluşturmadığını, oysa 3,5-MeO-PEAI tuzunun tavlama ile 2D katman oluşturduğunu ortaya koymuştur. Hem fotolüminesans hem de empedans spektroskopisi ölçümleri, tuz pasivasyonu ile rekombinasyonun azaldığını ve bunun da V_{OC}'de bir artışa yol açtığını göstermiştir. 3,5-MeO-PEAI tuzunun eklenmesiyle 1,14 eV kadar yüksek bir V_{OC} değeri elde edilmiştir, ancak 2,6-MeO-PEAI tuzuna sahip hücreler, referans hücrelerin

verimliliğini aşarak en iyi genel performansı sergilemiştir. Güç dönüştürme verimliliği (PCE), referans hücre için %18,14 iken, 2,6-MeO-PEAI tuzu ilavesinden sonra %19,15 değerine yükselmiştir. Ayrıca, tuzla işlem görmüş cihazların nem direnci, temas açısı ölçümleriyle kanıtlandığı üzere, büyük ölçüde iyileştirilmiştir. Üretimden altı hafta sonra, referans hücre ve 2,6-MeO-PEAI ve 3,5-MeO-PEAI uygulanan hücreler, ilk verimlerinin sırasıyla %77, %93 ve %94'ünü korumuştur, bu da tuz pasivasyonunun uzun süreli stabiliteyi geliştirdiğini açıkça göstermiştir.

Anahtar Kelimeler: Perovskit Güneş Hücresi, 3D/2D Perovskit, Arayüz Pasivasyonu, Organik Aralayıcı Katyonlar

To My Beloved Family

ACKNOWLEDGMENTS

I would like to express my deepest gratitude to my supervisor Professor Görkem Günbaş and co-supervisor Professor Selçuk Yerci for their guidance, advice, criticism, encouragements, and insight throughout the research. Their vision allowed me to constantly challenge myself and think of the bigger picture, which improved me greatly. I could not have completed my thesis without their valuable support. I would like to thank all members of the FLAIR LAB and Advanced Photonics Photovoltaics (APP). I am very grateful to Esra Bağ for supporting me in every step with her valuable advice and companionship. I would like to thank Gülsüm Güneş for teaching me the production steps and guiding me with patience throughout my research. I would also like to thank Elif Kirdeciler for her valuable ideas, support, and friendship. I would like to express my gratitude to Büşra İleri for photoluminescence measurements, absorbance measurements and her support. I would like to express my sincere thanks to Cem Şahiner for impedance measurements and his friendship. I would also like to thank Bahri Eren Uzuner for teaching me the electrical measurements and his support. I would like to thank Parisa Sharif for her supports, and Figen Varlıoğlu for the synthesis of novel cations. It was a great pleasure to be in this group and I could not imagine a better group to work with. In addition, I am glad to the Central LAB, especially to Pelin Paşabeyoğlu for GIXRD measurements and Dr. İlker Yıldız for UPS measurements. I would like to thank the ODTÜ-GÜNAM facility for allowing me to operate several laboratory instruments. This work was partially funded by Scientific and Technological Research Council of Turkey under grant number TÜBİTAK 118M061. I would like to thank everyone who contributed to and supported this project. Last but not the least, I would like to express my deepest gratitude to my spouse, Utku Yıldırım and my family, Dilek Çel, Mehmet Çel and Beril Çel Atabeyoğlu for constantly supporting and encouraging me.

TABLE OF CONTENTS

LIST OF TABLES

TABLES

LIST OF FIGURES

FIGURES

LIST OF ABBREVIATIONS

ABBREVIATIONS

AM1.5G	Air Mass 1.5 Global
AVAI	Aminovaleric Acid Iodide
BA	n-Butylamine
BAI	Butylammonium Iodide
BnAI	Benzylammonium Iodide
CB	Chlorobenzene
DAI	Dodecylammonium Iodide
DI	Deionized
DMF	Dimethylformamide
DMSO	Dimethyl Sulfoxide
E_g	Band Gap Energy
EAI	Ethylammonium Iodide
EQE	External Quantum Efficiency
ETL	Electron Transport Layer
FA	Formamidinium
FAMA	Formamidinium Methylammonium
FAPI	Formamidinium Lead Iodide
FF	Fill Factor
FTO	Fluorine-Doped Tin Oxide

GIXRD	Grazing Incidence X-Ray Diffraction
GuaI	Guanidinium Iodide
HI	Hysteresis Index
HOMO	Highest Occupied Molecular Orbital
HTL	Hole Transport Layer
I_{SC}	Short-Circuit Current
IAI	Imidazolium Iodide
IE	Ionization Energy
IPA	Isopropyl Alcohol
ITO	Indium Tin Oxide
J_{SC}	Short-Circuit Current Density
J-V	Current Density-Voltage
LED	Light-Emitting Diode
Li-TFSI	Bis(trifluoromethane) Sulfonimide Lithium
MA	Methylammonium
MAPI	Methylammonium Lead Iodide
MEAI	2-Methoxyethylammonium Iodide
MeO	Methoxy
MPP	Maximum Power Point
MPPT	Maximum Power Point Tracking
NMAI	1-Naphthylmethylamine Iodide
NREL	National Renewable Energy Laboratory

o-PDEAI$_2$	Ortho-(phenylene)di(ethylammonium) Iodide
OA	Octylammonium
OPV	Organic Photovoltaics
PAI	Phenylammonium Iodide
PCE	Power Conversion Efficiency
PEAI	Phenylethylammonium Iodide
PL	Photoluminescence
PMAI	Phenylmethylammonium Iodide
PSC	Perovskite Solar Cell
PV	Photovoltaic
R_S	Series Resistance
R_{Sh}	Shunt Resistance
RH	Relative Humidity
RT	Room Temperature
SQ	Shockley-Queisser
SR	Spectral Response
SRH	Shockley-Read-Hall
tBBAI	4-tert-Butyl-Benzylammonium Iodide
TBP	4-tert-Butyl Pyridine
TCI	Tokyo Chemical Industry
TCO	Transparent Conducting Oxide
TOAC	Tetraoctylammonium Chloride

TPA-PEABr	N-((4-(N,N,N-Triphenyl)Phenyl)Ethyl)Ammonium Bromide
TTMAI	Thieno[3,2-b]thiophen-2-ylmethanaminium Iodide
UPS	Ultraviolet Photoelectron Spectroscopy
UV	Ultraviolet
V_{OC}	Open-Circuit Voltage
VBM	Valence Band Maximum
2D	2-Dimensional
3D	3-Dimensional
3FBAI	Trifluoro-Substituted Butylammonium Iodide

LIST OF SYMBOLS

SYMBOLS

c	Speed of light
D	Crystallite size
E	Energy
h	Planck constant
I	Current
J	Current density
k	Rate constant
K	Crystallite shape factor
M	Molarity
n	Ideality factor / Electron charge carrier density / Number of layers
P	Power
q	Electronic charge
r	Effective radius
R	Resistance
S	Photon flux
t	Goldschmidt tolerance factor
T	Temperature
V	Voltage
β	Width of the X-ray diffraction peak

θ	Bragg angle
λ	Wavelength
ν	Frequency
Φ	Work function

CHAPTER 1

INTRODUCTION

Increasing energy demand has encouraged researchers to search for alternative, clean and sustainable energy sources. Among the renewable energy sources such as wind, tidal, solar, hydrothermal, geothermal; solar energy is the most promising one due to its abundance and capability to fulfill very high energy demands. For this purpose, photovoltaic (PV) solar cells were invented to convert sunlight into electricity.

In 1839, the photovoltaic effect was discovered by Edmond Becquerel. In 1873, Willoughby Smith observed and reported the photoconductivity in selenium. This was followed by Charles Fritts, who was the inventor of the first working PV cell which was based on selenium wafers. He also installed the world's first solar panel on a New York rooftop in 1884. In 1905, Albert Einstein presented the theory of the photoelectric effect and later on, he was awarded the Nobel Prize in Physics for this work in 1922. In 1946, Russell Shoemaker Ohl discovered the semiconductor solar cell and the p-n junction. Breakthrough of solar cells was achieved in 1954, when the world's first practical silicon solar cell with 6% efficiency was discovered by the scientists in Bell Laboratories.[1] This was the beginning of the first generation of solar cells, which was based on crystalline silicon. Since then, researchers have been investigating more materials to utilize low-cost solar cells, which gave rise to the second generation of solar cells. These cells were mostly based on III-V semiconductors such as cadmium telluride and copper indium gallium selenide.[2] Due to the scarcity and toxicity of these materials, third generation of solar cells emerged with the introduction of dye-sensitized solar cells and organic photovoltaics (OPV). Among the third generation, perovskite solar cells (PSCs) are the most promising ones due to their outstanding PV performance, abundancy, easy and low-cost processing.[3]

The history and development of PSCs, working principle and device architectures, and the performance parameters of PSCs are briefly explained in the following sub-sections. Moreover, challenges in the PSC research field as well as possible solutions are presented by focusing on interface engineering and low-dimensional perovskites. Lastly, the aim of the thesis is stated in this chapter.

1.1 Perovskite Solar Cells

A natural mineral, calcium titanate ($CaTiO_3$) was discovered by Gustav Rose in 1839. This mineral was named after Lev Perovski, who was a Russian mineralogist. Perovskite structure refers to any material with the same crystal structure as $CaTiO_3$.[4]

In general, perovskites have ABX_3 structure, where 'A' is a monovalent cation, 'B' is a divalent cation and 'X' is an anion that binds to both. For perovskite solar cells, 'A' is usually methylammonium (MA, $CH_3NH_3^+$) or formamidinium (FA, $CH(NH_2)_2^+$), 'B' is usually lead (Pb^{2+}) and 'X' is usually halide such as iodine (I^-), bromine (Br^-) or chlorine (Cl^-). The ideal perovskite structure is the cubic structure, as can be seen in Figure 1.1.[5]

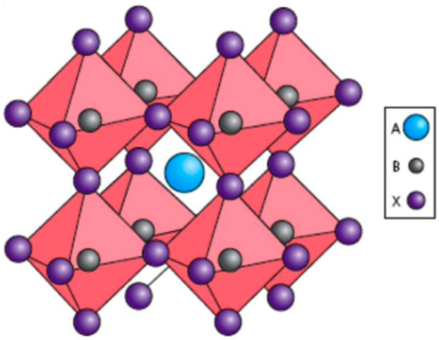

Figure 1.1. Perovskite crystal structure[6]

The crystallographic structure of perovskite and its stability are determined by the Goldschmidt tolerance factor, t, for which the formula is given below.[6]

$$t = \frac{r_A + r_X}{\sqrt{2}(r_B + r_X)} \qquad (1.1)$$

In this formula, r_A, r_B and r_X represent the effective radii of the corresponding ions. In general, the tolerance factor for perovskite crystals is in the range $0.8 \leq t \leq 1$, where t being 1 indicates a perfect cubic system. The condition $t < 0.8$ means that A site cation is too small, whereas the condition $t > 1$ means that A cation is too large. Both conditions suppress the formation of perovskite and may lead to different crystal structures.[7]

There are various advantages of perovskites. The possibility to form many different structures by changing A, B and X ions creates a huge family of perovskites, as shown in Figure 1.2. This leads to an amazing property of perovskites, which is the fact that their band gap can be tuned by changing A, B and X compounds.[8] Due to the unique properties of perovskites such as having a direct band gap, high absorption coefficients, low exciton binding energy and large dielectric constant, they can be used for variety of optoelectronic applications such as lasers,[9] light-emitting diodes,[10] transistors,[11] and solar cells.[12]

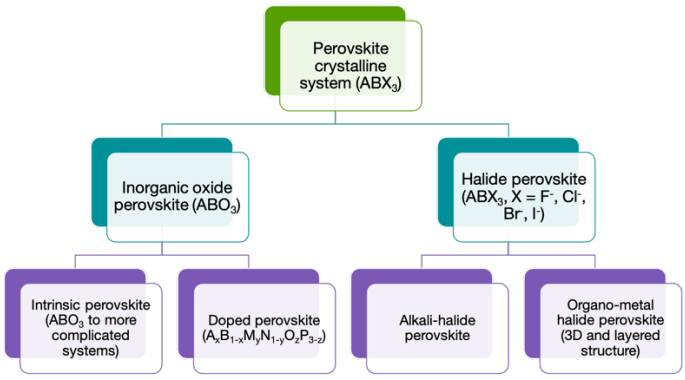

Figure 1.2. Perovskite crystalline system; reproduced from [8]

1.1.1 Brief History and Development of Perovskite Solar Cells

In 2009, the first perovskite solar cell (PSC) was produced using $MAPbI_3$ and $MAPbBr_3$ in dye-sensitized solar cell configuration.[13] The power concersion efficiency (PCE) of these cells was around 3%, however their stability was very poor due to the liquid electrolyte. In 2011, cell structures with quantum dots were created with $MAPbI_3$.[14] These cells had better performance, however they also suffered from instability due to the liquid electrolyte. In 2012, the first all-solid-state PSC was created with 9.7% efficiency, where the liquid electrolyte was replaced with a solid hole conductor, namely 2,2′,7,7′-tetrakis[N,N′-di(4-methoxyphenyl)amino]-9,9′-spirobifluorene (Spiro-OMeTAD).[15] This was a milestone for the progress of PSCs since these cells were both efficient and stable. This work was followed by many researchers who utilized different perovskite structures, deposition techniques and materials, resulting in a remarkable increase in PCE. To this day, the highest efficiency is reported as 25.7% according to the best research cell efficiency chart published by the National Renewable Energy Laboratory (NREL),[16] which is very close to the highest efficiency achieved with silicon solar cells. The progress of PSCs, and their efficiency values compared with that of silicon solar cells can be seen in Figure 1.3.[17]

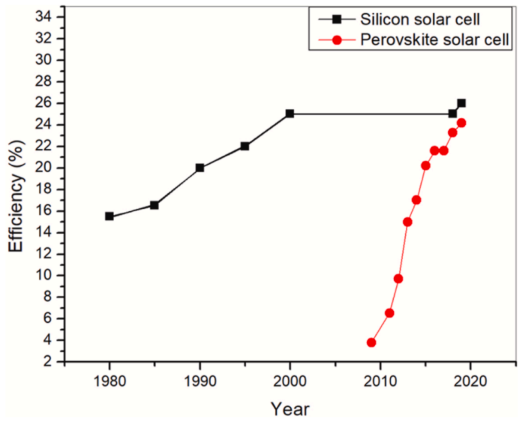

Figure 1.3. Recorded PCE of PSCs compared to silicon solar cells in years[17]

1.2 Working Principle and Device Architecture

Perovskite solar cells function similar to the solid-state p-n junction solar cells. Upon light exposure on PSCs, perovskite layer absorbs photons of wavelength matching its band gap. With the absorption of photons, electrons are excited to the conduction band of perovskite, leaving holes in the valence band, which are also treated as charge carriers. These electrons and holes are collected by the electron transport layer (ETL) and the hole transport layer (HTL), respectively. Free electrons pass from the perovskite layer to the ETL and arrive at the transparent conducting oxide (TCO), which is usually indium tin oxide (ITO), or fluorine doped tin oxide (FTO). Simultaneously, holes travel to the HTL and arrive at the metal electrode. TCO and metal electrodes are connected resulting in the electron flow through the external circuit which generates the photocurrent, and recombination of electrons and holes in the end.[18] The schematic of this process is illustrated in Figure 1.4.

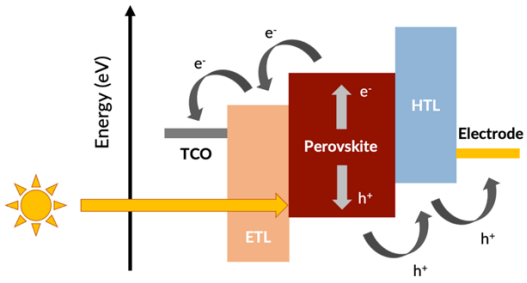

Figure 1.4. Electron and hole generation in PSCs

PSCs can be fabricated in mesoporous or planar structures. In mesoporous structure, perovskite material is attached to a mesoporous metal oxide scaffold layer. The function of this scaffold is to help photogenerated electrons transfer to the ETL. This structure requires high temperature treatment processes during fabrication.[19] Although the mesoporous device structure was commonly used in the early discoveries, the planar structure attracted more attention lately due to its simplicity.[20] Typical planar device structure consists of a perovskite absorber layer, sandwiched between an HTL and an ETL, with a TCO and metal electrodes.[21] Planar structure can have two different configurations. In regular (n-i-p) planar structure, n-type ETL

is coated on top of the TCO, and the light reaches the ETL first, whereas in inverted (p-i-n) structure, p-type HTL is coated on top of the TCO, and the light reaches the HTL first.[22] Representative schematics of the different device architectures can be seen in Figure 1.5.

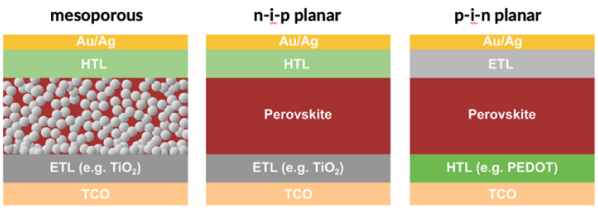

Figure 1.5. Device architecture of PSCs[19]

The device performance is highly related with the choice of transport layers. Transport layers with efficient charge extraction and good transport properties lead to a high-performance cell. A good transport layer must have properties such as proper band alignment with perovskite, high transmittance in the visible region, high carrier mobilities, high stability, easy and low-cost processability.[23]

The ETL extracts and transports photogenerated electrons from perovskite to the TCO or the metal electrode, while blocking the hole transport. In addition, the ETL plays a role in the surface modification of the perovskite film and charge recombination mitigation.[24] The ETL must have compatible energy levels with the perovskite in order to facilitate electron transport and enhance the built-in potential.[25] The most commonly used ETLs are titanium dioxide (TiO_2) and tin oxide (SnO_2) for the n-i-p structure, and [6,6]-phenyl-C61-butyric acid methyl ester ($PC_{61}BM$) for the p-i-n structure. Other than these materials, fullerene and its derivatives, metal oxides, small organic molecules, and polymers are also used as ETLs.[26] Electron extraction and transport properties of ETLs can further be improved by doping, passivation and using additives or nanoparticles.[27] The HTL transports photogenerated holes from the perovskite to the metal electrode or the TCO, while blocking the electron transport. It reduces charge recombination which results in an increase in selectivity of the contact, and an enhancement of the open-circuit voltage.[28] In addition, the

HTL may prevent the degradation of the cell, since it may act as a moisture resistant layer or metal ion diffusion barrier. Moreover, it facilitates a better coverage of the perovskite layer.[29] The most commonly used HTLs are Spiro-OMeTAD and poly[bis(4-phenyl) (2,5,6-trimethylphenyl)amine] (PTAA) for the n-i-p structure, and poly (3,4-ethylene dioxythiophene):poly (4-styrenesulfonate) (PEDOT:PSS) for the p-i-n structure. Besides these materials, small molecules, polymers, and inorganic molecules are also used as HTLs. Energy levels of some common ETLs and HTLs with respect to perovskites are shown in Figure 1.6.[30]

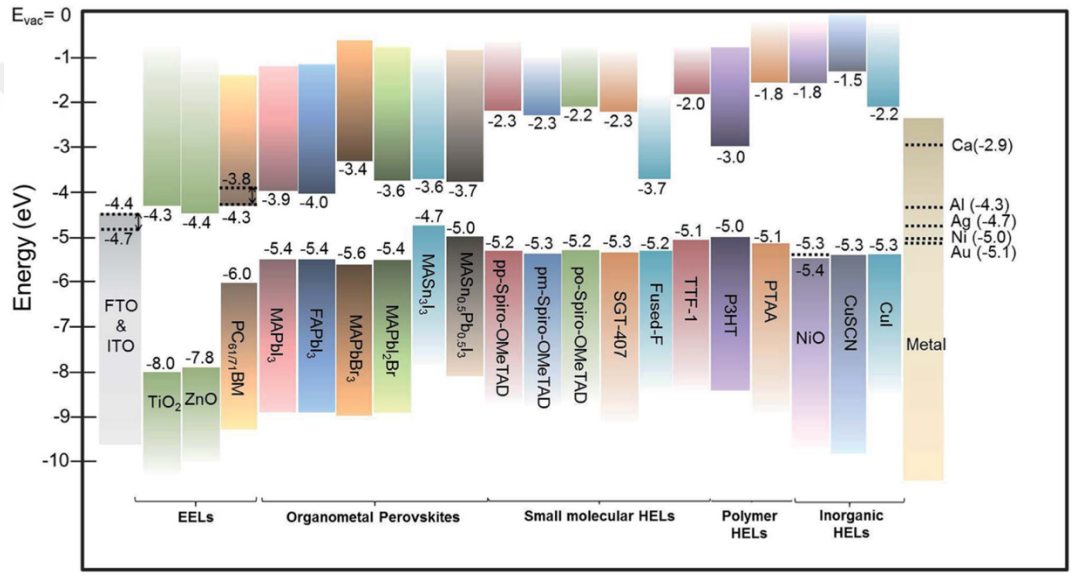

Figure 1.6. Schematic representation of energy levels of various ETLs and HTLs[30]

1.3 Operational Parameters

The efficiency of a solar cell is determined by some operational parameters, which are measured over against a standard reference spectrum under standard test conditions. The standard reference spectrum is identified as Air Mass 1.5 global (AM1.5G). Standard test conditions designate a total irradiance of 1 sun to be 100 mW/cm^2 and an operating temperature of 25 °C.[31]

Operational parameters of solar cells are identified by the current density-voltage (J-V) graph, which is the superposition of the J-V curve of the cell diode in the dark with the light-generated current.[32] J-V graph of a solar cell, as shown in Figure 1.7, provides information about its main performance parameters, which are short-circuit current density (J_{SC}), open-circuit voltage (V_{OC}), fill factor (FF) and power conversion efficiency (PCE).

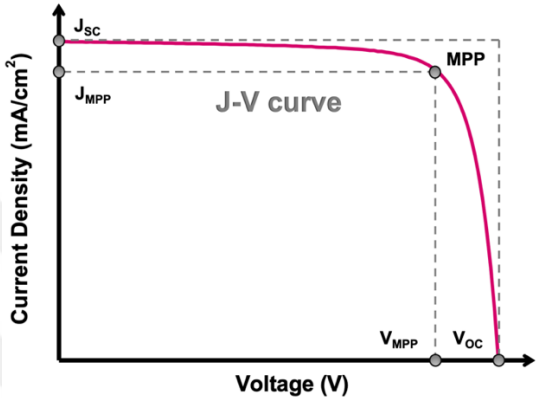

Figure 1.7. Typical J-V curve of a solar cell

J_{SC} is defined as the ratio of short-circuit current (I_{SC}) to the active area of the solar cell. I_{SC} is the maximum current from a solar cell and occurs when the net voltage across the device is zero. I_{SC} depends on the area of the cell, number of photons, the spectrum of the incident light, and optical properties and the collection probability of the cell. To eliminate the area dependence, J_{SC} is commonly used.[33]

V_{OC} is the maximum voltage from a cell and occurs when the net current through the device is zero. V_{OC} is formulated by the following equation:

$$V_{OC} = \frac{nkT}{q} \, ln\left(1 + \frac{I_L}{I_0}\right) \qquad (1.2)$$

where kT/q represents the thermal voltage, T is the temperature, n is the ideality factor, I_0 is the dark saturation current, and I_L is the light produced current.[33]

Maximum power point (MPP) is defined as the point at which the cell could demonstrate the maximum power output (P_{max}), which is formulated as:

$$P_{max} = V_{MPP} \times J_{MPP} \qquad (1.3)$$

where V_{MPP} and J_{MPP} is the voltage and the current density at the maximum power point, respectively.

FF is defined as the ratio of maximum power generated by a cell to the product of V_{OC} and J_{SC}.[34]

$$FF = \frac{V_{MPP} \times J_{MPP}}{V_{OC} \times J_{SC}} \qquad (1.4)$$

In other words, FF is equal to the inner square, shown in Figure 1.7 with dashed lines, divided by the outer square. According to this, FF should be equal to one in an ideal solar cell, however in reality, FF is typically in the range of 0.50-0.82 and around 0.80 for a classical silicon PV system. FF is highly dependent on the series resistance (R_S), shunt resistance (R_{Sh}) and diode losses. R_S is mainly due to the resistance created in the top and rear metal contacts, whereas R_{Sh} is due to the defects that occur during fabrication. Increasing R_{Sh} while reducing R_S will result in enhanced FF and thus, higher cell efficiency.[35]

From these parameters, PCE is defined as the ratio of energy output from a solar cell to input energy from the sun.[33]

$$PCE = \frac{P_{out}}{P_{in}} = \frac{V_{OC} \times J_{SC} \times FF}{P_{in}} \qquad (1.5)$$

The predicted theoretical PCE limit of a perovskite solar cell is about 31%. This value is very close to the calculated Shockley-Queisser (SQ) limit,[36] that is 33%, achievable by gallium arsenide solar cells.[37]

1.4 Challenges in Perovskite Solar Cells

Despite the superior advantages of perovskite solar cells, there are still some drawbacks that need to be overcome. The main problem of PSCs is the instability nature of perovskites. Perovskites are highly sensitive materials that can be affected by air, moisture, heat, and light. The most stable PSC is reported to have one year of lifetime, whereas it is more than 25 years for silicon solar cells.[38] Another challenge is the hysteresis phenomena observed during the J-V measurement of solar cells. Extensive research is being carried on with the aim of achieving stable and hysteresis-free PSCs that may lead to commercialization. These challenges as well as the solution proposals are explained in detailed in the following sub-sections.

1.4.1 Stability

The stability of the solar cells is determined by standard tests, some of which are light soaking at elevated temperatures, temperature cycling (-40 to 85 °C) and thermal and relative humidity (RH) tests (at 85 °C and 85% RH).[39] Moreover, according to the standards of thin-film photovoltaic cells, their PCE losses should be a maximum of 10% of their initial yields over a period of 1000 h.[40]

Perovskite solar cells suffer from stability problems caused by both the intrinsic instability of perovskite and the extrinsic instability related to the ambient conditions. Extrinsic instability caused by oxygen and humidity, and intrinsic instability caused by light, heat and electrical bias may lead to the degradation of PSCs.

Moisture induces chemical reactions that break the hydrogen bonds in the perovskite structure and form hydrated compounds, which cause the degradation of the perovskite material. Many reports are published suggesting that water is the catalyst for the irreversible degradation. The proposed degradation process of $CH_3NH_3PbI_3$ ($MAPbI_3$) perovskite along with the chemical reactions is shown in Figure 1.8. Even though these reactions are reversible, at the time when the perovskite gets saturated by the moisture, the process will be irreversible and $MAPbI_3$ will be degraded into

MAI and PbI_2.[41] Several approaches have been proposed to increase the moisture resistance of PSCs, such as using a HTL that blocks moisture, employing a thin blocking layer between the perovskite and HTL, and using hydrophobic carbon electrode.[42]

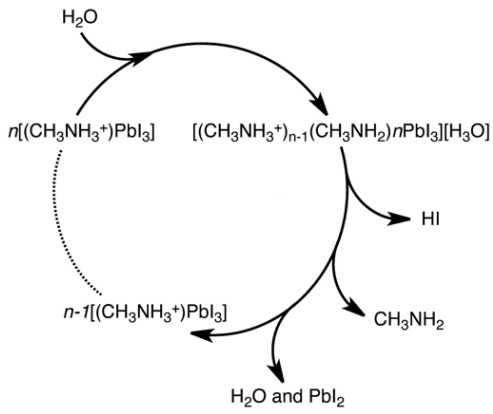

Figure 1.8. Moisture-induced degradation pathway of $MAPbI_3$ perovskite[41]

Oxygen in the environment can react with the ions of MA^-, Pb^+, I^- in the perovskite structure, that creates electronic traps and charge barriers. In addition, oxygen molecules may create Pb-O bonds on the film surface that leads to the degradation of PSCs. The detrimental impacts of oxygen as well as moisture can be largely reduced by the encapsulation of PSCs.[43]

Heat also induces reversible and irreversible chemical reactions of the degradation of the perovskite, which can be seen below. $MAPbI_3$ perovskite can be decomposed at 85 °C under an inert atmosphere.[44] Furthermore, at around 54-57 °C, $MAPbI_3$ perovskite experiences a phase transition from the tetragonal to cubic phase, changing the tolerance factor (t). If t value gets out of the optimal range, thermal effects can cause degradation due to lattice distortion.[45] Additionally, heat may have severe effects on the organic layers in the device stack. Most of the organic HTLs, including the commonly used HTL, Spiro-OMeTAD suffer from thermal instability. Mixed halide perovskites and replacing organic cations with inorganic cations[46] as well as enhancing transport layer properties are suggested to increase the thermal stability of PSCs.

$$CH_3NH_3PbI_3(s) \overset{\Delta}{\Leftrightarrow} CH_3NH_2(g) + HI(g) + PbI_2(s) \quad (1.6)$$

$$CH_3NH_3PbI_3(s) \overset{\Delta}{\rightarrow} CH_3I(g) + NH_3(g) + PbI_2(s) \quad (1.7)$$

$MAPbI_3$ perovskite can also undergo a photochemical degradation induced by light illumination. High-energy photons may break the chemical bonds in $MAPbI_3$ perovskite, which leads to the decomposition of $MAPbI_3$ into PbI_2 and MAI. MAI then decomposes into CH_3NH_2, HI and/or I_2. Light illumination not only decomposes the perovskite, but also degrades some of the materials employed in the device structure, such as Spiro-OMeTAD. In order to solve this problem, suitable, low-light induced degradable perovskites and transport layers need to be chosen and employed in PSCs.[43]

Several strategies are proposed to enhance the long-term stability of PSCs, such as encapsulation, compositional engineering of perovskite materials, multidimensional perovskites, solvent engineering, interface engineering and passivation.[47] Some of the most promising solutions, interface engineering and multidimensional perovskites, are covered in Sections 1.5 and 1.6, respectively.

1.4.2 Hysteresis

Current density-voltage (J-V) responses of PSCs may exhibit abnormal dependence on the voltage scan direction and speed, which is defined as hysteresis. In other words, hysteresis is the phenomena of the difference in PCE in forward and reverse scans during the J-V measurement. Generally, PCE in forward scan is lower than that in reverse scan.[48] Hysteresis also depends on p- and n-type contact material, as well as the device architecture.[49] Additionally, it is revealed that the n-i-p structure exhibits much more severe hysteresis than the p-i-n structure.[50] This behavior makes it difficult to determine the accurate PCE of the cells.

Some possible causes of hysteresis are ferroelectric polarization, slow transient capacitive current, charge traps at the interface and grain boundaries, and ion migration.[51] The ferroelectric polarization process is much faster than the hysteresis process. Trapping and detrapping processes occurring at the interface and grain boundaries is also unlikely to be the main source of hysteresis due to the long duration and current decay magnitude. Therefore, ion migration theory gets more attention among the other causes.[52] Ion migration defines a situation when the ions of the perovskite, usually the iodide (I^-) ions, move towards to the ETL or HTL interfaces under different voltage bias. This movement leaves vacancies at the interfaces, which induce energy band bending within the perovskite layer and the two interfaces. Variation of energy barrier leads to different V_{OC} and PCE values under different voltage bias, which is observed as hysteresis effect in the J-V measurement.[53]

To describe the degree of hysteresis for a solar cell, hysteresis index (HI) is usually reported, which is given in the formula below. HI should be minimum for an ideal cell.[54]

$$HI = \frac{PCE_{reverse} - PCE_{forward}}{PCE_{reverse}} \qquad (1.8)$$

The aforementioned methods to improve stability of PSCs, which are interface engineering, compositional engineering, selective contact engineering, perovskite bulk defect engineering and multidimensional perovskites are also effective to reduce the hysteresis effect.[55]

1.5 Interface Engineering

In PSCs, there are inevitable defects and carrier transport barriers at the interface, which lead to charge accumulation and recombination. Carrier recombination occurring in the bulk or at the ETL/perovskite or perovskite/HTL interfaces results

in a decrease in V_{OC} and FF such that they are much less than the theoretical maximum values.[56]

The main recombination processes in PSCs are Shockley-Read-Hall (SRH) recombination (also known as trap-assisted or defect-assisted recombination), radiative recombination (also known as band-to-band recombination), and Auger recombination, which are illustrated in Figure 1.9.[57]

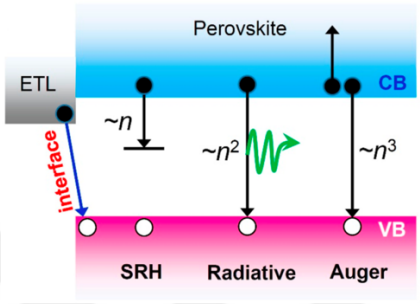

Figure 1.9. Schematic illustration of the recombination processes in PSCs

Charge carrier recombination in semiconductors is expressed as the following relation:

$$\frac{dn}{dt} = -k_1 n - k_2 n^2 - k_3 n^3 \qquad (1.9)$$

where n is the electron charge carrier density, k_1, k_2, and k_3 are the rate constants for SRH, radiative, and Auger recombination processes, respectively.[58] V_{OC} and FF may reach the theoretical maximum value when there is only the radiative recombination process, and they tend to decrease upon the contribution of SRH and Auger recombination, which are nonradiative recombination.[59] Auger recombination has a negligible effect on PSCs under 1 sun illumination. Therefore, SRH recombination, which depends on the energy level depth and the density of defects, dominates the main nonradiative recombination loss in PSCs.[60]

In addition to the bulk defects, interface defects also exist in PSCs, which lead to interfacial nonradiative recombination losses.[61] The interface defects are mainly

under-coordinated Pb^{2+} ions, Pb cluster, iodine vacancies, organic A cation vacancy, and under-coordinated I^- ions, which are shown in Figure 1.10.[62] Moreover, defects may cause ion migration, which was previously discussed to cause hysteresis phenomena, and have influence on the long-term stability of the cell.[63] Therefore, surface defect passivation achieved by interface engineering is crucial to minimize the interfacial losses, which hinder the development of PSCs in terms of both efficiency and stability.

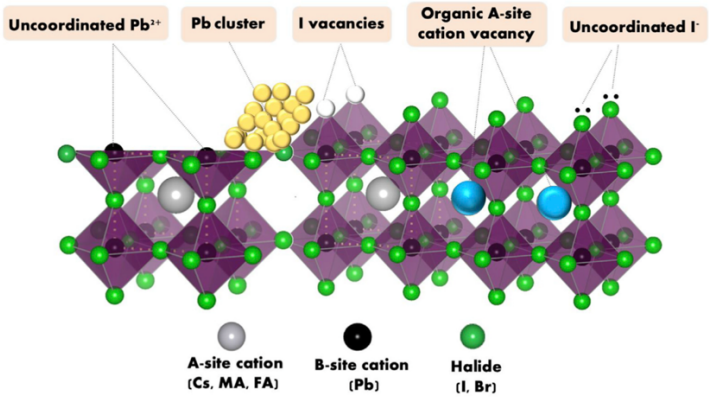

Figure 1.10. The possible surface defects of the perovskite layer[62]

Several surface passivation strategies are reported so far, including passivation via Lewis bases,[64] thin protective capping layer,[65] organic ammonium halide salts,[66] low-dimensional perovskites.[38] These strategies can be applied to one or more of the interfaces in PSCs, which are ETL/perovskite, perovskite/HTL, cathode/ETL, HTL/anode, as well as grain boundary inside the perovskite layer. The modification of perovskite/HTL interface is widely studied.[67] For the purpose of this thesis, the improvements of the perovskite/HTL interface passivation by post treatment after the formation of perovskite are included and summarized in the following.

Fullerene and its derivatives, which can act as Lewis acids, can be used for the surface passivation of perovskite films. From the work of Shao et al. PCBM was proven to reduce recombination and hysteresis by passivating both surface and bulk defects.[68] Lewis acids were shown to play an active role in the passivation of undercoordinated I^- defects by halogen bonding[69,70] and the moisture stability.[71]

Chaudhary et al. proposed a hydrophobic polymer, poly(4-vinylpyridine) to passivate the undercoordinated Pb atoms by its pyridine Lewis base side chains.[72] Thiophene derivatives were also proven to improve charge transfer and collection at the interface by taking the advantage of having highly delocalized π-electrons from the thiophene ring.[73,74] Lin et al. introduced a π-conjugated Lewis base, indacenodithiophene end-capped with 1.1-dicyanomethylene-3-indanone, into the PSCs and proposed the Lewis adduct that was formed by the coordination between the carbonyl and cyano groups in the Lewis base with the Lewis acid defects on the perovskite film surface.[75] Moreover, perovskite surface passivation as well as suppressed ion migration were successfully achieved with 2-mercaptopyridine molecule,[76] methimazole molecule,[77] and a bifunctional molecule consisting of the mercapto-tetrazolium (S) and phenyl ammonium (N) moieties.[78]

The formation of wide band gap inorganic oxide capping layer onto the perovskite film is another surface passivation strategy in order to reduce recombination and improve stability. Yang et al. proposed a post-treatment of the perovskite film with sulfate or phosphate ions, which resulted in the wide band gap lead oxysalt layers that passivated the undercoordinated Pb clusters and improved the stability.[79] Another example is the post-treatment with hydrogen peroxide reported by Godding et al. This treatment formed the PbO layer on top of the perovskite surface by oxidizing Pb^0, which inhibited the formation of vacancies and improved the device performance.[80] Similarly, the formation of hydrophobic organic capping layer onto the perovskite film is also used as a passivation strategy. Small molecules with fluorine groups can be used as a passivation and moisture blocking layer due to the hydrogen bonds between the strongly electronegative fluorine with water molecules.[81,82]

Using organic ammonium salts is another widely used passivation strategy. These materials passivate the defects of the perovskite film by hydrogen or ionic bonding, and they may either form a capping low-dimensional perovskite layer on top of the 3D perovskite, or merely passivate the defect states.[83] Passivation effect of organic

ammonium salts is reviewed in the following, and low-dimensional perovskite applications are explained in Section 1.6.

Zhao et al. proposed diammonium salts to passivate the perovskite surface, and demonstrated that the treatment with $NH_3I(CH_2)_8NH_3I$ could reduce the defect density and enhance the performance, whereas the treatment with $NH_3I(CH_2)_4NH_3I$ and $NH_3I(CH_2)_2O(CH_2)_2NH_3I$ did not improve the performance due to the 3D to 2D perovskite phase transformation.[66] Jung et al. further proposed that octylammonium (OA) did not form a 2D perovskite layer due to the high formation energy, contrary to butylammonium and phenylethylammonium, which formed 2D layered structures. The post-treatment with OA cation led to the formation of encapsulated individual 3D perovskite domains, which not only reduced the nonradiative recombination but also enhanced the device stability.[84] Alharbi et al. introduced ethylammonium iodide (EAI), imidazolium iodide (IAI), and guanidinium iodide (GuaI) on top of the perovskite layer to reduce the defects. Great enhancement in V_{OC} and FF was achieved with EAI treatment, exhibiting a stabilized PCE of 22.3%.[85] In addition to reducing the defect density and suppressing the nonradiative recombination, organic ammonium salts can also promote the dispersion of PbI_2 on the perovskite surface into a discontinuous thin layer. By employing butylammonium iodide (BAI) and trifluoro-substituted butylammonium iodide (3FBAI), Jiang et al. demonstrated the enlargement of the passivation effect of excess PbI_2.[86] You and coworkers reported the passivation of FAMA perovskite with phenylethylammonium iodide (PEAI) salt that achieved a superior V_{OC} of 1.18 V and a certified PCE of 23.32%. It was also demonstrated that upon annealing, the passivation effect of PEAI was lost because of the 2D perovskite formation.[87] Zhu et al. showed that using a tailored amphiphilic molecule, 4-tert-butyl-benzylammonium iodide (tBBAI), as a passivation material resulted in an efficiency of 23.5%, by improving charge extraction due to the tert-butyl groups that hindered the molecular aggregations on the perovskite film surface.[88] Gunes et al. demonstrated an enhanced PCE and superior stability upon the post-treatment of FAMA perovskite with thieno[3,2-b]thiophen-2-ylmethanaminium iodide molecule.[89] Nazeeruddin and coworkers employed ortho-,

meta- and para-isomers of phenylene diethylammonium iodide, and demonstrated that the treatment with ortho-isomer, that was the most sterically hindered, exhibited the best passivation effect by preventing the 2D perovskite formation, even at elevated temperatures.[90] Photovoltaic parameters and stability information of the best-performing PSCs reported in the literature are summarized in Table 1.1, which only includes the articles that involve perovskite passivation with organic ammonium salts, without the formation of a 2D layer, in the n-i-p structure.

Table 1.1. Reported champion device performances and stability data of n-i-p type PSCs with perovskite passivation by organic ammonium salts

Perovskite	**Passivation Molecule**	**V_{OC} (V)**	**J_{SC} (mA/cm^2)**	**FF (%)**	**PCE (%)**	**Stability**	**Ref**
MAPI	PEAI:MAI BAI:MAI	1.08 1.08	18.63 16.56	73.00 62.00	14.94 11.49	Storage in 75% RH for 19 days. Retained PCE: ~76% (for PEAI:MAI)	91
FAPI	Benzylamine	1.12	23.60	73.00	19.20	Stable in air (~50% RH) for 4 months	92
MAPI	OA	1.11	22.60	81.50	20.60	Heat test at 85 °C in ambient for 760 h. Retained PCE: 80%	84
CsFAMA	EAI IAI GuaI	1.12 1.15 1.12	24.14 23.85 24.50	81.00 79.00 75.00	22.40 22.11 21.00	MPPT under continuous illumination for 550 h. Retained PCE: 95% (for EAI)	85
FAMA	PEAI	1.18	25.20	78.40	23.32	Heat test at 85 °C for 500 h. Retained PCE: ~80%	87
CsFAMA	tBBAI	1.14	25.10	82.10	23.50	MPPT for 500 h, and storage in 50-70% RH in ambient for 55 days. Retained PCE: 95%, and 90%, respectively	88
FAMA	TPA-PEABr	1.09	23.13	72.00	18.15	Storage in 40-50% RH at RT for a month. Retained PCE: 80%	93

Table 1.1 (Cont'd)

FAMA	TTMAI	1.11	22.47	80.52	20.16	Storage in ~15% RH for 380 h. Retained PCE: 82%	[89]
CsFAMA	o-PDEAI$_2$	1.16	24.75	83.50	23.92	Storage in 40-50% RH for 1008 h, and MPPT in inert for 1100 h. Retained PCE: 85%, and 90%, respectively.	[90]
FAMA	BAI 3FBAI	1.15 1.15	24.93 24.71	76.49 75.33	22.01 21.32	Storage in 85% RH at RT for 1100 h. Retained PCE: ~90%	[86]
CsFAMA	TOAC	1.13	24.29	77.12	21.24	Storage in air (40-55% RH) for 720 h. Retained PCE: 97%	[94]

1.6 Low-Dimensional Perovskites

Low-dimensional perovskites draw attention due to their unique optoelectronic properties and superior stability. Low-dimensional perovskites are obtained when long alkyl chained A site spacer cations are introduced into the 3-dimensional (3D) perovskites. This leads to tolerance factor becoming larger than 1 because spacer cations have a large ion radius.[95] Low-dimensional perovskites are generally expressed in the formula of $(A')_mA_{n-1}B_nX_{3n+1}$, where A' can be a divalent (m = 1) or monovalent (m = 2) cation.[96] In this formula, n is the number of metal layers that are sandwiched between the organic layers. Band gap and quantum confinement tuning can be managed by changing n. A pure 2-dimensional (2D) layer is achieved when n = 1, whereas a pure 3D perovskite layer is formed when n = ∞. All other possibilities when $1 < n < \infty$ correspond to the quasi-2D perovskites, which are illustrated in Figure 1.11. For the 2D Ruddlesden-Popper perovskites, m = 2, thus the general formula is $(A')_2A_{n-1}B_nX_{3n+1}$.[97]

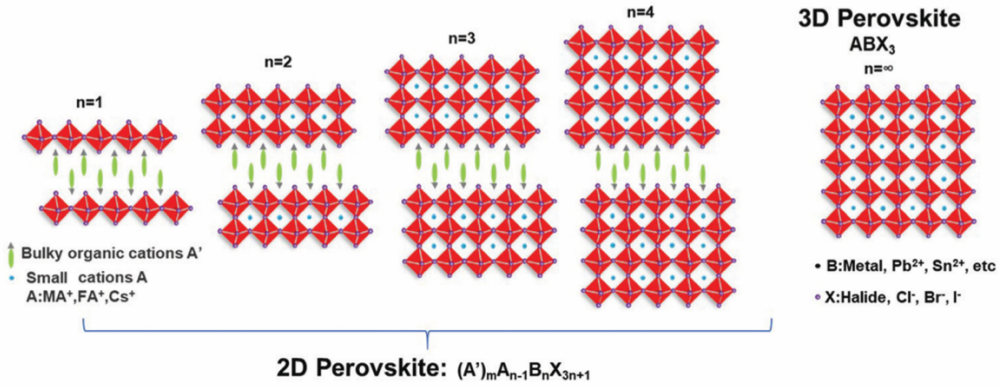

Figure 1.11. Schematic illustration of 2D, quasi-2D and 3D perovskite structures[96]

Low-dimensional perovskite layers are generated by cutting along the <100>, <110> or <111> crystallographic planes of the 3D perovskite, which results in three different structures, as shown in Figure 1.12. Among these structures, <100> oriented perovskites are the most commonly used ones in PSCs.[98]

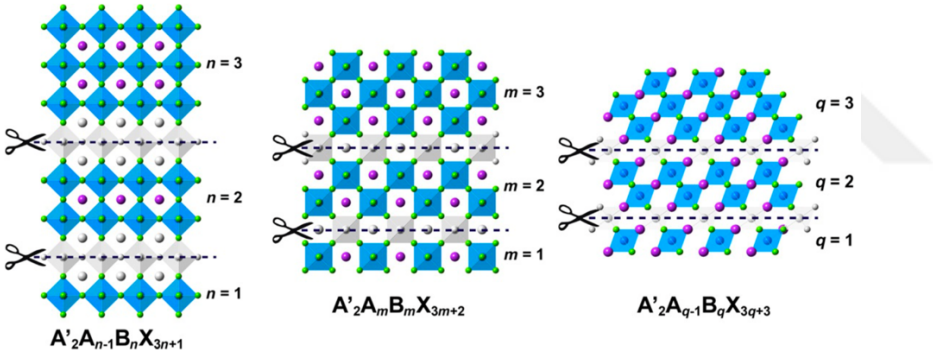

Figure 1.12. Low-dimensional perovskites from cutting along different planes[98]

Organic spacers, that are bulky aliphatic or aromatic alkylammonium cations, are used to create 2D perovskite layers. 2D perovskites are reported to exhibit superior moisture resistance due to the hydrophobicity of organic cations. Furthermore, 2D perovskites can form high quality films with enhanced surface coverage and fewer grain boundaries.[99] On the other hand, the introduction of bulky organic cations may have adverse effects on charge carrier transportation if the energy band levels of these cations are not aligned in the structure.[100]

Even though the solar cells with 2D perovskites display great stability, studies have shown that their efficiencies fall behind in the PSC research field due to their wide band gaps and large exciton binding energies. The advantages of both 2D and 3D perovskites can be exploited by employing 2D perovskites as passivation layers on top of 3D perovskites, which is widely used as an interface passivation strategy for stability improvement and defect passivation.[101] The following criteria should be taken into consideration when forming a 2D layer onto the 3D perovskite: 1) the bulky cation must be at an appropriate size to fit into the A' site, 2) primary ammonium cations are preferred as spacers to coordinate with the [PbI_6] octahedra, 3) elevated temperatures may be required for the formation of the 2D phase.[102] Creation of 3D/2D multidimensional perovskites with bulky organic salts are widely used in the literature, which are reviewed in the following.

The concept of mixed 3D/2D perovskite-based PSCs was first demonstrated by Smith et al. They proposed to mix a large PEA cation with MA cations to form the quasi-2D perovskite structure (n = 3), which resulted in a high V_{OC} of 1.18 V. Furthermore, the cells exhibited great long-term stability and moisture resistance when stored in air with 52% of RH for 46 days.[103] Nazeeruddin and coworkers reported one-year stable (zero loss for over 10000 h) 3D/2D PSCs by employing aminovaleric acid iodide (AVAI).[38] Koh et al. proposed butylammonium iodide (BAI) and octylammonium iodide (OAI) to form 3D/2D heterojunction and reported lower trap state densities, indicating defect passivation, thereby reduced nonradiative recombination. Moreover, the 3D/2D cells exhibited enhanced ambient stability and moisture resistance due to the hydrophobic nature of the long aliphatic carbon chains.[104] Kim et al. further demonstrated the effect of the alkyl chain length on the cell performance by employing BAI, OAI, and dodecylammonium iodide (DAI) on FAMA perovskite. As the alkyl chain length increased, the electron-blocking effect and humidity resistance were reported to increase significantly. OAI-treated PSC displayed a stabilized PCE of 22.9%, whereas DAI-treated device exhibited superior moisture and heat resistance.[105] Park and coworkers fabricated 3D/2D PSCs by using phenylammonium iodide (PAI), phenylmethylammonium iodide (PMAI), and

phenylethylammonium iodide (PEAI) and reported that V_{OC} increased with increasing alkyl chain length. PEAI treatment was reported to result in a reduced nonradiative recombination as well as increased carrier lifetime. It was also shown that a blue shift in the PL peak appeared after PEAI treatment, which was ascribed to the 2D perovskite, however, XRD data was not presented to support the 2D layer formation on top of the 3D perovskite.[106] PEAI and BAI bulky cations were reported to form 3D/2D structure, on the other hand, 2D formation was not observed when PAI cation was used, as demonstrated by Ghoreishi et al. Interestingly, the lowest recombination and the highest performance was seen for the PAI-treated cells.[107] Jen and coworkers proposed using PEAI, 4-fluoro-phenylethylammonium iodide (F-PEAI), and 4-methoxy-phenylethylammonium iodide (MeO-PEAI) to create quasi-2D PSCs, and showed that F-PEAI-treated perovskite (n = 5) displayed the highest PCE due to the enhanced charged transport properties and lower band gap.[108] Zhou et al. further investigated the influence of fluorination position, that were ortho-, meta-, para-, of F-PEAI spacer on the PSC performance. It was shown that ortho-F-PEAI-treated cells displayed the highest V_{OC} (1.21 V) and PCE due to forming stronger hydrogen bonds with the 3D perovskite.[109] It was also reported that the electron density on the benzene ring varies with different functional groups attached, which has significant effect on the passivation of surface defects.[110] MeO-PEAI treatment is proven to form highly efficient 3D/2D perovskite films by improved defect passivation effect, enhanced charge carrier transport, as well as increased moisture resistance.[110,111] PV parameters and stability information of the best-performing 3D/2D PSCs reported in the literature are summarized in Table 1.2, which only includes the articles that involve passivation with bulky organic salts in the n-i-p structure.

Table 1.2. Reported champion device performances and stability data of n-i-p type 3D/2D PSCs with bulky organic salts

Perovskite	Passivation Molecule	V_{OC} (V)	J_{SC} (mA/cm^2)	FF (%)	PCE (%)	Stability	Ref
CsFAMA	BAI OAI	1.06 1.02	19.40 19.37	76.69 76.70	15.74 15.19	Storage in 50% RH for 100 h. Retained PCE: 86% (for BAI)	[104]
MAPI	BA BAI	1.11 1.09	22.49 22.59	78.00 77.00	19.56 18.85	Heat test at 95 °C for 100 h. Retained PCE: 96.5% (for BA) and 88.2% (for BAI)	[112]
FAMA	BAI OAI DAI	1.11 1.12 1.13	23.99 24.08 23.97	81.70 81.80 81.00	21.71 22.03 21.89	Storage in 65% RH at 65 °C for 100 h. Retained PCE: 80% (for DAI)	[105]
CsFA	PAI PMAI PEAI	0.98 1.02 1.04	23.18 22.85 23.16	72.60 74.20 75.50	16.47 17.32 18.09	Storage in ambient (20% RH at RT) for 120 h. Retained PCE: 95% (for PEAI)	[106]
FAMA	PEAI CH_3-PEAI MeO-PEAI NO_2-PEAI MEAI	1.13 1.16 1.18 1.06 1.08	24.64 24.49 25.04 23.36 23.79	75.27 76.94 77.79 66.68 69.07	20.96 21.85 22.98 16.51 17.74	Storage in ambient (20-30% RH at RT) for 1000 h. Retained PCE: ~100% (for MeO-PEAI)	[110]
MAPI	PEAI BAI PAI	1.01 1.02 1.02	21.80 22.10 22.20	80.00 80.00 80.00	17.50 17.60 18.20	Not reported	[107]
CsFAMA	ortho-F-PEAI meta-F-PEAI para-F-PEAI	1.17 1.18 1.15	22.62 22.75 22.23	77.90 76.80 79.50	20.60 20.52 20.37	Storage in ambient (10-20% RH at RT) for 2 months. Retained PCE: 95% (for o-F-PEAI), 94% (for m-F-PEAI), 99% (for p-F-PEAI)	[109]

Table 1.2 (Cont'd)

CsFAMA	BnAI	1.08	24.48	78.80	20.79	MPPT under continuous illumination for 600 h. Retained PCE: 80%	[113]
CsFAMA	NMAI	1.18	22.98	77.34	21.04	Storage in ambient (~30% RH) for 3240 h. Retained PCE: 98.9%	[114]
MAPI	MeO-PEAI	1.10	24.87	71.80	19.64	Storage in ambient (35% RH) for 230 h. Retained PCE: 50%	[111]
FAMA	CF_3-PEAI	1.11	24.25	78.21	21.05	Storage in ambient (70-80% RH) for 528 h. Retained PCE: 98%	[115]

1.7 Aim of the Thesis

The purpose of this thesis was to investigate the effects of introducing two novel cations, namely 2,6-methoxy-phenylethyl ammonium iodide (2,6-MeO-PEAI) and 3,5-methoxy-phenylethyl ammonium iodide (3,5-MeO-PEAI), into the solar cell structure. Herein, the cations were used on top of $(FAPbI_3)_{1-x}(MAPbBr_3)_x$ (FAMA) perovskite as passivation layers with the aim of passivating the perovskite layer by diminishing the defect density and reducing nonradiative recombination. Furthermore, the effect of annealing after the cation treatment was investigated in detail. Grazing incidence X-ray diffraction measurements were conducted to check whether a pure 2D perovskite layer was formed. Recombination characteristics were analyzed with photoluminescence and impedance spectroscopy measurements. Additionally, light stability, long-term stability, and moisture stability of the devices were examined with maximum power point tracking under constant light illumination, current density-voltage tracking, and contact angle measurement, respectively.

CHAPTER 2

FABRICATION AND CHARACTERIZATION TECHNIQUES

In this chapter, materials used in the experiments, synthesis of novel cations as well as the experimental procedure are explained in detail. Moreover, device characterization techniques such as current density-voltage, external quantum efficiency, maximum power point tracking, impedance spectroscopy, and thin film characterization techniques such as grazing incidence X-ray diffraction, photoluminescence, ultraviolet photoelectron spectroscopy, contact angle are elucidated in this chapter. In addition, instruments used in the experiments are also included in the sub-sections.

2.1 Materials

SnO_2 colloid solution (tin (IV) oxide, 15% in H_2O colloidal dispersion) was purchased from Alfa Aesar. Formamidinium iodide (FAI) and methylammonium bromide (MABr) were purchased from Greatcell Solar, and methylammonium chloride (MACl) were purchased from Lumtec. Lead iodide (PbI_2) was provided from Tokyo Chemical Industry (TCI). Isopropyl alcohol (IPA), 2,2′,7,7′-tetrakis[N,N′-di(4-methoxyphenyl)amino]-9,9′-spirobifluorene (Spiro-OMeTAD), bis(trifluoromethane) sulfonimide lithium salt (Li-TFSI), 4-tert-butyl pyridine (TBP), and chlorobenzene (CB) were procured from Sigma Aldrich. Dimethylformamide (99.9%) (DMF) and dimethyl sulfoxide (99.9%) (DMSO) were provided from Acros Organics.

2.2 Synthesis of Novel Cations

Two novel cations, that are 2,6-methoxy-phenylethylammonium iodide (2,6-MeO-PEAI) and 3,5-methoxy-phenylethylammonium iodide (3,5-MeO-PEAI) were successfully synthesized with a molecular weight of 309.15 g/mol by Figen Varlıoğlu. The synthesis routes and structures of these cations are shown in Figure 2.1. The detailed synthesis procedure of the novel cations are explained in the thesis of Figen Varlıoğlu.

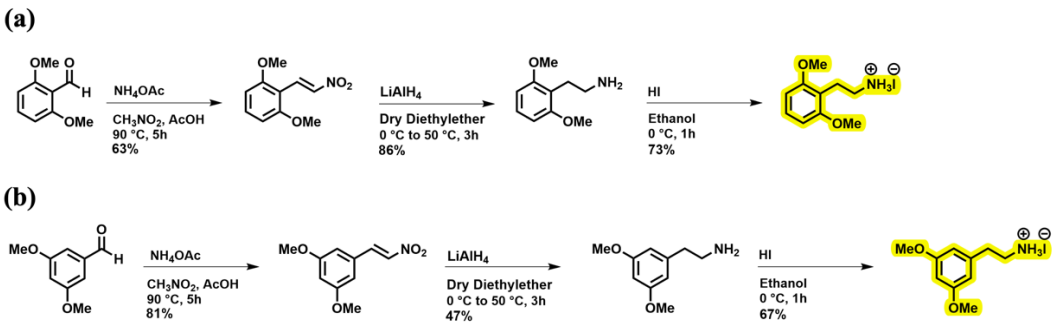

Figure 2.1. The synthesis routes and structures of novel cations (a) 2,6-MeO-PEAI, (b) 3,5-MeO-PEAI

2.3 Fabrication of Perovskite Solar Cells

Perovskite solar cells were fabricated in the planar n-i-p architecture, with the structure of glass/FTO/SnO_2/FAMA/Salt/Spiro-OMeTAD/Ag, as shown in Figure 2.2. The reference cells did not contain the salt layer.

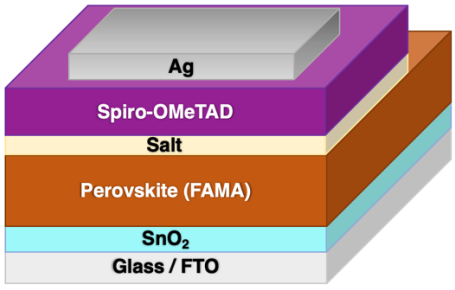

Figure 2.2. The schematics of the device architecture

As the first step of the fabrication procedure, glass substrates coated with FTO (7 ohms/sq) were etched with zinc powder and 4 M hydrochloric acid (HCl). After etching, substrates were cleaned in the ultrasonic cleaner with Hellmanex, deionized (DI) water, acetone, and IPA for 15 minutes, respectively. Then, substrates were subjected to ultraviolet (UV)-ozone treatment for 10 minutes. The diluted SnO_2 solution (2.14% in DI water) was coated on substrates at 4000 rpm for 30 seconds, followed by thermal annealing at 150 °C for 30 minutes. After cooling, samples were subjected to another UV-ozone treatment for 20 minutes and transferred into the N_2-filled glovebox. PbI_2 solution was prepared by dissolving 1.3 M in DMF:DMSO (95:5) (v/v) mixture and stirring at 70 °C for 3 hours. FAMA solution was prepared by dissolving FAI:MACl:MABr (60:6:6 mg) in 1 mL of IPA and stirring at 70 °C for 30 minutes. The spin-coating was performed by a sequential method, in which PbI_2 solution was coated and annealed at first, followed by FAMA solution coating and annealing. PbI_2 solution was coated at 1500 rpm for 30 seconds and annealed at 70 °C for 1 minute. FAMA solution was coated at 1300 rpm for 30 seconds and annealed at 150 °C for 15 minutes. Novel cations, that are 2,6-MeO-PEAI and 3,5-MeO-PEAI were dissolved in IPA with different concentrations and spin rates, followed by annealing at 100 °C for 5 minutes. For hole transport layer, Spiro-OMeTAD solution was prepared by dissolving 72.3 mg of Spiro-OMeTAD in 1 mL of CB. 17.5 μL Li-TFSI (520 mg/mL in acetonitrile) and 28.8 μL TBP was added into the solution as dopants. Finally, 120 nm of silver was deposited on the substrates in the thermal evaporator under high vacuum. For each experimental set, the same fabrication procedure was followed. The schematics of the fabrication procedure can be seen in Figure 2.3.

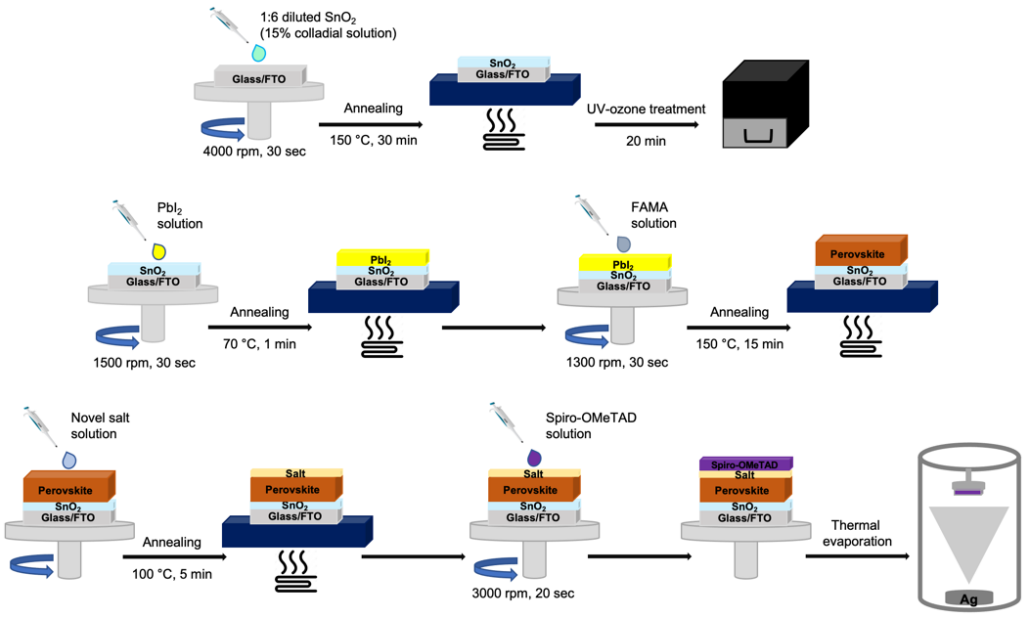

Figure 2.3. The schematics of the fabrication procedure

2.4 Device Characterization

This section includes the theory and tools used for the current density-voltage (J-V), external quantum efficiency (EQE), maximum power point tracking (MPPT), and impedance spectroscopy measurements, that were performed for the electrical characterization of the solar cells.

2.4.1 Current Density-Voltage

Current density-voltage (J-V) measurements, that reveal the performance parameters of the cells, were performed by Keithley 2400 source meter, and Pico G2V LED solar simulator under AM1.5G with 100 mW/cm^2 illumination intensity with a scan rate of 100 mV/s. For J-V measurements, polycrystalline silicon shadow masks were used with 3 mm^2 designated as the active area of metal contacts. Devices were measured in the laboratory under ambient air with relative humidity of ~20-40% at room temperature.

2.4.2 Maximum Power Point Tracking

Maximum power point tracking (MPPT) measurements were performed to analyze the light stability of the solar cells. MPPT measurements were conducted in the same system as in J-V measurements, which were performed by Keithley 2400 source meter, and Pico G2V LED solar simulator under AM1.5G with 100 mW/cm^2 illumination intensity with a scan rate of 100 mV/s. During MPPT measurements, devices were in the laboratory (in ambient air with relative humidity of ~20-40%, at room temperature) under a constant illumination of 1 sun.

2.4.3 External Quantum Efficiency

The external quantum efficiency (EQE) is defined as the ratio between the number of charge carriers collected by the cell with the number of incident photons. The spectral shape of EQE reveal the efficiency of photocurrent generation process and may provide insight on the loss mechanisms within the cell. To determine EQE, the spectral response (SR) needs to be defined, which is the ratio of the current generated by the cell to the incident power. EQE is formulated as:

$$EQE(\lambda) = \frac{hc}{q\lambda} \times SR \qquad (2.1)$$

where, h is the Planck constant (6.63 x 10^{-34} J.s), c is the speed of light (3.0 x 10^8 m/s), q is the electronic charge, and λ is wavelength.[116]

The measured EQE at a specific wavelength is utilized to find the integrated short-circuit current density (J_{SC}). The integrated J_{SC} can be calculated from the following equation:

$$J_{sc} = \int qEQE(\lambda)S(\lambda)d\lambda \qquad (2.2)$$

where, q is the elementary charge, and S(λ) is the photon flux.[116]

In addition, any incoming light that has a lower energy, or a longer wavelength, than the band gap energy, cannot be absorbed by the cells.[116] Thus, in the EQE spectrum, where the EQE value drops to zero, band gap can be inferred from the following equation:

$$E_g = \frac{hc}{\lambda} \qquad (2.3)$$

where, E_g is the band gap energy, and h times c is calculated as 1240 eV.[117]

EQE measurements were performed by a PV characterization system (Bentham Instruments, PVE300) equipped with a light source and monochromator, where solar cells were operated under the short-circuit condition and the current was measured for each wavelength. Then, the raw data of the current was normalized, and the integrated J_{SC} values of the cells were automatically calculated.

2.4.3.1 Current Density-Voltage Correction

During the optimization experiments, explained in Sections 3.1.1 and 3.1.2 under Chapter 3, high J_{SC} values were obtained in J-V measurements for all devices. The best-performing devices were seen to have J_{SC} values exceeding 26 mA/cm^2, as shown in Table 3.2. To check whether the J_{SC} values were correct, EQE measurement was conducted with the best-performing devices.

Generally, J_{SC} obtained from EQE measurements is found to be slightly lower than J_{SC} obtained from J-V measurements. This may be due to the fact that a typical EQE setup uses a Xe lamp with a monochromator as the light source. Therefore, the light intensity from the EQE light source at a given wavelength is low compared to the standard 1 sun illumination used in the solar simulator in the J-V setup. This leads to a variation in the charge density in the device, which can raise the mismatch of the J_{SC} values obtained from EQE and J-V measurements. A J_{SC} decrease up to 10% is

considered to be acceptable in EQE measurements, providing J_{SC} obtained from J-V measurements is reasonably correct.[118]

Herein, J_{SC} found from EQE measurements was much lower and not consistent with J_{SC} found from J-V measurements, therefore, J-V correction was done in the Keithley software. This J-V correction was the reason of the decrease in J_{SC} and PCE values in the sections following Section 3.1.2. The corrected J_{SC} and PCE values were calculated and included in the Tables 3.1 and 3.2. After the correction, J_{SC} mismatch was eliminated, which is shown in Section 3.1.2.1.

2.4.4 Impedance Spectroscopy

Impedance measurements were performed with the aim of analyzing the characteristics of recombination and charge carrier transportation processes. The measurements were conducted using MFIA Impedance Analyzer (Zurich Instruments) in the frequency range between 10 Hz to 1 MHz with an oscillation peak amplitude of 15 mV. Cells were operated under the open-circuit condition. A DC blocking capacitor was connected to the signal output of the impedance analyzer. The true oscillation voltage across the cell was sensed via 4-terminal measurement mode. The cells were illuminated with a light-emitting diode (LED) with a wavelength of 625 nm (Thorlabs M625L4), which was calibrated by the short-circuit photocurrent of a sample cell, corresponding to an equivalent of 0.1 Suns AM1.5G.

2.5 Film Characterization

This section includes the theory and tools used for the grazing incidence X-ray diffraction (GIXRD), photoluminescence (PL), ultraviolet photoelectron spectroscopy (UPS), and contact angle measurements, that were performed for the surface characterization of thin films.

2.5.1 Grazing Incidence X-Ray Diffraction

Grazing incidence X-ray diffraction (GIXRD) measurements were performed to investigate the difference in the crystal structure of the reference and the cation-treated films. The GIXRD patterns were obtained using a Rigaku Ultima-IV X-Ray diffractometer with Cu Kα radiation at 30 kV and 40 mA operation conditions. A grazing angle of 0.5° and a scan rate of 2°/min were used as operating parameters. The crystallite size of the grains is determined by the Debye-Scherrer Equation:

$$D = \frac{K\lambda}{\beta cos\theta} \qquad (2.4)$$

where, D is crystallite size, K is the crystallite shape factor (generally regarded as 0.9), λ is the wavelength of the X-ray, β represents the full width at half maximum of the X-ray diffraction peak, and θ is the Bragg angle.[119]

2.5.2 Photoluminescence

Photoluminescence (PL) measurements were performed with the aim of investigating charge transport and passivation effects upon salt treatment. PL measurements were conducted in the setup that was designed in our laboratory. PL setup consists of two Ocean Insight Tungsten Halogen light sources, two Ocean Insight flame visible/near-infrared spectrometer, UV-visible bifurcated fibers, which are high OH fibers that transmit the light (300-1100 nm) efficiently, UV-visible

patch cords, and two collimating lenses. In PL measurements, the samples were excited from the glass side with an excitation wavelength of 430-435 nm using a UV-LED lamp. The radiation of the excited sample was detected by the reflection probe.

2.5.3 Ultraviolet Photoelectron Spectroscopy

Ultraviolet photoelectron spectroscopy (UPS) measurements were performed to gain insight on the energy level alignment. In UPS measurements, He-I discharge lamp was used as the light source with a photon energy of 21.22 eV. In the measurements, a bias of 7 eV was applied. The positions of the valence band maxima were assigned using linear extrapolation of the leading edge of the valence band emissions. The secondary electron cut-off energy ($E_{cut\text{-}off}$ or E_0) is at the low kinetic energy onset, whereas the valence band maximum energy is at the high kinetic energy onset of the spectrum. The work function can be calculated from the following equation, in which h represents the photon energy, that is 21.22 eV.[120]

$$\phi = h\nu - E_{cut-off} \qquad (2.5)$$

Ionization energy (IE) is determined by the following equation:

$$IE = \phi + (E_{VBM} - E_F) \qquad (2.6)$$

where, E_F is the Fermi level energy, which was assumed to be positioned at zero eV, and E_{VBM} is the valance band energy.[120]

2.5.4 Contact Angle

Contact angle measurements were performed to investigate the effect of salt treatment on hydrophobicity. The Attension Theta Lite software was used for the measurements and water was used as the solvent, revealing moisture stability of the cells.

CHAPTER 3

RESULTS & DISCUSSION

Experiments were conducted in order to see the effect of two novel cations in the performance of PSCs. For both salts, concentration and spin rate optimizations were done systematically, which can be seen in the following sub-sections in this chapter. The value ranges chosen for optimization studies were decided based on literature and previous reports. After the optimization studies, two salts were used with their optimal values for comparison in the same experimental set, in which the salt annealing effect was also investigated. Grazing incidence X-ray diffraction (GIXRD), photoluminescence (PL), ultraviolet photoelectron spectroscopy (UPS), impedance spectroscopy and external quantum efficiency (EQE) characterizations were done to investigate this set. Additionally, 2D only and quasi-2D films were fabricated and analyzed in GIXRD measurements for further investigation. Lastly, light and moisture stability of the cells, as well as their long-term stabilities were reported in the following sub-sections.

3.1 Optimization of 2,6-MeO-PEAI

2,6-MeO-PEAI salt optimization was done systematically. Optimum concentration of the salt was chosen at first. Then, spin rate for the salt coating step was optimized. Lastly, experiments were done in order to decide the correct salt annealing temperature.

3.1.1 Concentration Optimization

For the concentration optimization, 1 mg, 2 mg, 3 mg and 4 mg of 2,6-MeO-PEAI salt was dissolved in IPA and coated with a spin rate of 3000 rpm on top of the

perovskite layer, whereas there was no salt in the reference devices. Photovoltaic (PV) parameters of the cells are shown in Table 3.1. Due to the difference in J_{SC} values obtained by J-V and EQE measurements, which was explained in Section 2.4.3.1, J_{SC} and PCE values were corrected accordingly, and labeled as corrected values in Table 3.1. The cells treated with 2 mg/mL of salt concentration exhibited the best average PCE, which was slightly higher than the reference cell, mainly due to the enhancement in V_{OC}. A slight V_{OC} increase was observed for all the salt-treated solar cells.

Table 3.1. Photovoltaic parameters of PSCs with different concentrations of 2,6-MeO-PEAI

Devices		**V_{OC} (V)**	**J_{SC} (mA/cm^2)**	**FF (%)**	**PCE (%)**	**$J_{SC,\ corrected}$ (mA/cm^2)**	**PCE $_{corrected}$ (%)**
Reference	Average	1.10	24.50	75.96	20.48	21.15	17.67
	Highest	1.10	24.60	77.57	20.99	21.23	18.11
1 mg/mL	Average	1.12	24.10	75.78	20.38	20.80	17.65
	Highest	1.12	24.81	76.92	21.37	21.42	18.45
2 mg/mL	Average	1.12	24.45	76.39	20.84	21.11	18.06
	Highest	1.12	25.09	77.90	21.89	21.66	18.90
3 mg/mL	Average	1.11	23.90	77.27	20.55	20.63	17.69
	Highest	1.12	24.67	79.60	22.00	21.30	18.99
4 mg/mL	Average	1.09	23.54	75.46	19.44	20.32	16.71
	Highest	1.11	25.42	76.48	21.58	21.94	18.63

The statistical distribution graphs of the reference and salt-treated solar cells are given in Figure 3.1. From these graphs, it is evident that the cells treated with 2 mg/mL of salt displayed a narrower distribution of PV parameters, which indicated better uniformity compared to the other cells.

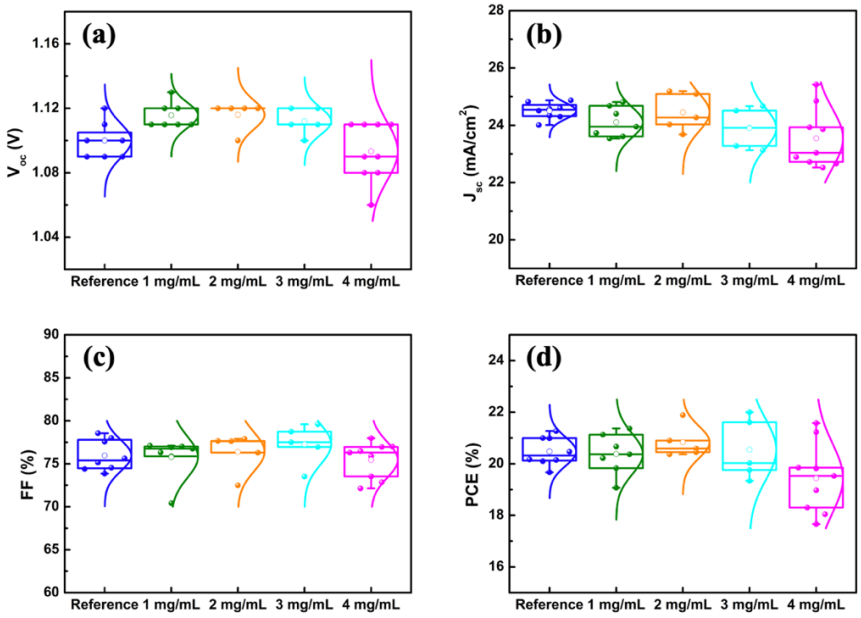

Figure 3.1. (a) V_{OC}, (b) J_{SC}, (c) FF, and (d) PCE statistics of PSCs with different concentrations of 2,6-MeO-PEAI

J-V curves of the best-performing devices can be seen in Figure 3.2. Before the J-V correction, the highest efficiencies were obtained as 20.99% (V_{OC} = 1.10 V, J_{SC} = 24.60 mA/cm^2, FF = 77.57%) for the reference device, 21.89% (V_{OC} = 1.12 V, J_{SC} = 25.09 mA/cm^2, FF = 77.90%) for the device treated with 2 mg/mL of salt, and 22.00% (V_{OC} = 1.12 V, J_{SC} = 24.67 mA/cm^2, FF = 79.60%) for the device treated with 3 mg/mL of salt. Although the device treated with 3 mg/mL of salt displayed the highest PCE, 2 mg/mL was chosen and used in the following experiments due to its higher average PCE and narrower statistical distribution of PV parameters.

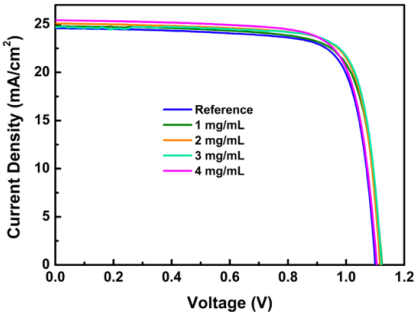

Figure 3.2. J-V curves of the best-performing devices with different concentrations of 2,6-MeO-PEAI

3.1.2 Spin Rate Optimization

Spin rate was another important parameter for the optimization of the salt coating step. 2,6-MeO-PEAI salt dissolved in IPA was coated with a spin rate of 500, 1000, 1500, 2000, 3000 and 4000 rpm on top of the perovskite layer, whereas the reference devices did not contain the salt layer. The salt-treated cells exhibited higher V_{OC} values than that of the reference cells, as shown in Table 3.2. Due to the difference in J_{SC} values obtained by J-V and EQE measurements, which was explained in Section 2.4.3.1, J_{SC} and PCE values were corrected accordingly and labeled as corrected values in Table 3.2. A significant V_{OC} increase was achieved with the treatment of 2,6-MeO-PEAI salt coated with 1500 rpm. The cells with the salt coating spin rate of 4000 rpm performed poorer than the other cells, probably due to the fact that 4000 rpm coating led to a layer of salt that was too thin.

Table 3.2. Photovoltaic parameters of PSCs with different spin rates of 2,6-MeO-PEAI

Devices		**V_{OC} (V)**	**J_{SC} (mA/cm^2)**	**FF (%)**	**PCE (%)**	**$J_{SC,\ corrected}$ (mA/cm^2)**	**PCE $_{corrected}$ (%)**
Reference	Average	1.10	24.48	73.58	19.79	21.13	17.10
	Highest	1.10	25.79	74.39	21.10	22.26	18.22
500 rpm	Average	1.12	23.80	75.61	20.18	20.54	17.39
	Highest	1.11	24.71	76.34	20.94	21.33	18.07
1000 rpm	Average	1.12	24.36	74.24	20.26	21.03	17.49
	Highest	1.12	26.48	74.84	22.19	22.86	19.16
1500 rpm	Average	1.13	24.55	76.50	21.14	21.19	18.32
	Highest	1.13	26.10	78.06	23.02	22.53	19.87
2000 rpm	Average	1.11	24.50	74.04	20.17	21.15	17.38
	Highest	1.12	25.32	74.12	21.02	21.86	18.15
3000 rpm	Average	1.12	24.49	73.84	20.18	21.14	17.48
	Highest	1.11	25.70	74.70	21.31	22.18	18.39
4000 rpm	Average	1.10	23.62	74.09	19.31	20.39	16.62
	Highest	1.11	24.45	75.08	20.38	21.11	17.59

The statistical distribution graphs of the reference and salt-treated solar cells were given in Figure 3.3. These graphs clearly indicated the enhancement, especially in V_{OC} and FF, when 1500 rpm was used as the salt coating speed. Superior V_{OC} and FF values of the cells with the salt coating spin rate of 1500 rpm had led to higher average and best PCE values. V_{OC} values peaked at 1500 rpm and increasing the spin rate further was seen to cause a decrease in V_{OC}.

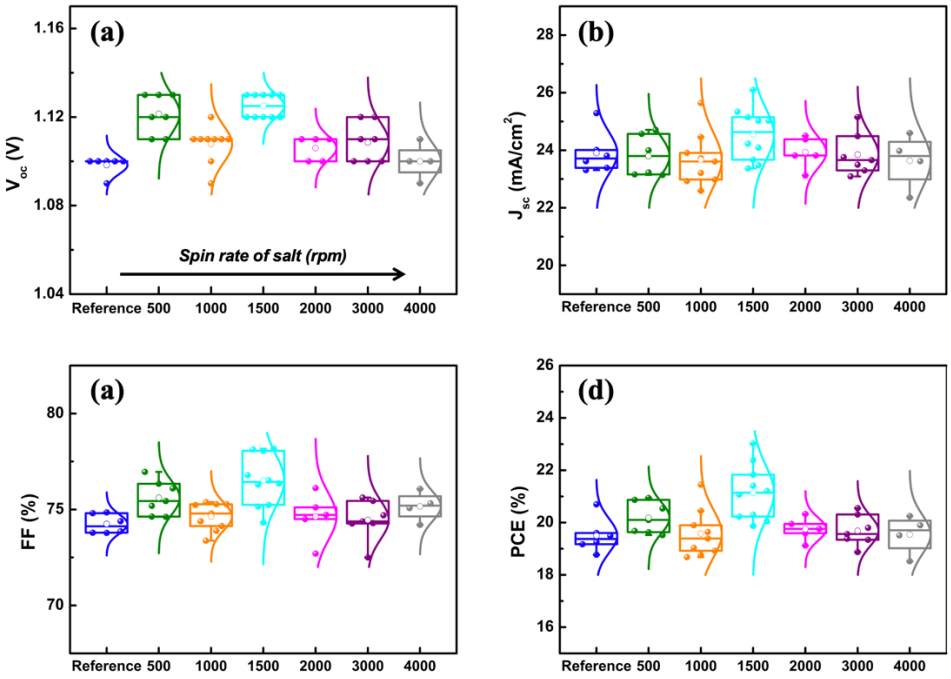

Figure 3.3. (a) V_{OC}, (b) J_{SC}, (c) FF, and (d) PCE statistics of PSCs with different spin rates of 2,6-MeO-PEAI

J-V curves of the best-performing devices are shown in Figure 3.4. Before the J-V correction, the highest efficiencies were obtained as 21.10% (V_{OC} = 1.10 V, J_{SC} = 25.79 mA/cm^2, FF = 74.39%) for the reference device, and 23.02% (V_{OC} = 1.13 V, J_{SC} = 26.10 mA/cm^2, FF = 78.06%) for the device with the salt coating spin rate of 1500 rpm. 1500 rpm was chosen as the optimum salt coating spin rate and used in the following experiments.

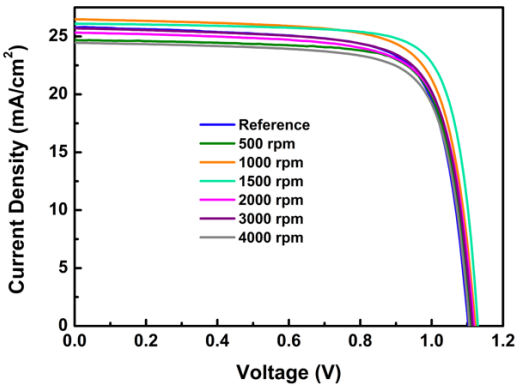

Figure 3.4. J-V curves of the best-performing devices with different spin rates of 2,6-MeO-PEAI

3.1.2.1 External Quantum Efficiency

Best performing devices were taken to EQE measurement, as shown in Figure 3.5. After the J-V correction, which was explained in Section 2.4.3.1, J_{SC} values obtained from the J-V measurement were 21.62 mA/cm^2 and 22.53 mA/cm^2 for the reference device and the device with the salt coating spin rate of 1500 rpm, respectively. Similarly, J_{SC} values obtained from the EQE measurement were 21.40 mA/cm^2 and 22.16 mA/cm^2 for the reference device and the device with the salt coating spin rate of 1500 rpm, respectively.

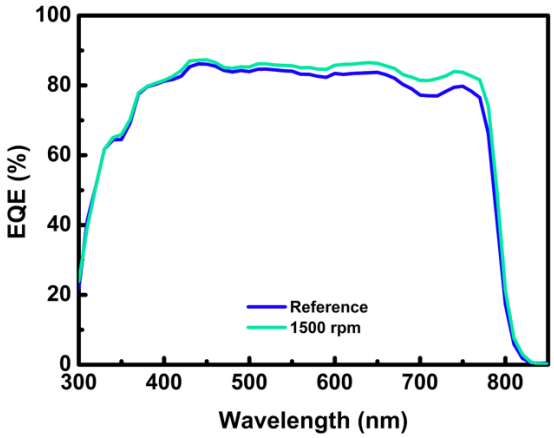

Figure 3.5. EQE spectra of the best-performing devices of the reference cell and the cell with the salt coating spin rate of 1500 rpm

3.1.2.2 Grazing Incidence X-Ray Diffraction

Samples were fabricated for grazing incidence X-ray diffraction (GIXRD) measurement in the structure of FTO/SnO_2/Perovskite/2,6-MeO-PEAI. 2,6-MeO-PEAI salt was coated with a spin rate of 500, 1000, 1500 and 2000 rpm on top of the perovskite layer, whereas the reference samples did not contain the salt layer. GIXRD measurement results are presented in Figure 3.6. A new peak occurred at around 6.27° upon salt addition. GIXRD peaks below 10° were commonly attributed to the formation of a low dimensional perovskite layer.[121] Thus, the new peak could be attributed to the possible 2D layer formation. GIXRD peaks were investigated in more detail under Chapter 3 in Section 3.3.2.1.1. The intensity of this new peak was much higher for the sample with the salt coating spin rate of 500 rpm, since a thicker salt layer was formed. Increasing the salt coating spin rate from 500 rpm to 2000 rpm, the intensity of this peak decreased as expected, because the thickness of the salt layer was reduced.

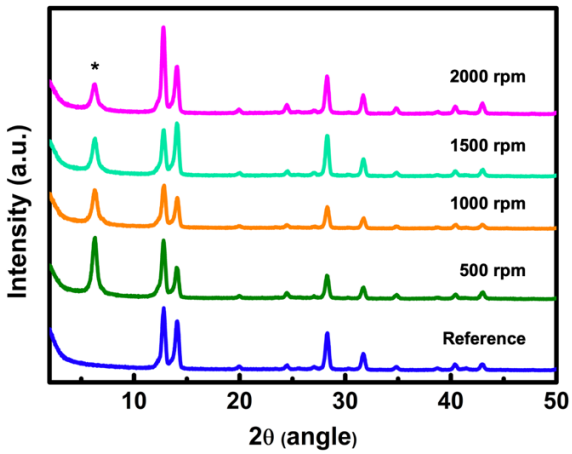

Figure 3.6. GIXRD patterns of the reference sample and samples with different spin rates of 2,6-MeO-PEAI; * represents the new peak at 6.27° upon salt addition

3.1.3 Annealing Temperature Optimization

The ideal annealing temperature for the salt annealing step was needed to be decided to further optimize the 2,6-MeO-PEAI salt. After coating the salt, cells were annealed at 100 °C in the previous experiments. For the salt annealing temperature optimization, 2,6-MeO-PEAI was coated on top of the perovskite layer and annealed at 80 °C, 100 °C, 120 °C and 140 °C. Moreover, cells that were not subjected to annealing after the salt coating step were also fabricated for comparison. The salt-treated cells that were annealed at 100 °C and 120 °C exhibited higher V_{OC} values than that of the other cells, as shown in Table 3.3. Comparing the PCE values of the annealed and non-annealed cells, salt annealing was revealed to be crucial for the device performance. On the other hand, elevating the annealing temperature higher than 120 °C was observed to be unfavorable for the solar cell performance. Cells that were annealed at 140 °C exhibited poorer performance due to decreased V_{OC} and FF.

Table 3.3. Photovoltaic parameters of PSCs with different salt annealing temperatures

Devices		V_{OC} (V)	J_{SC} (mA/cm^2)	FF (%)	PCE (%)
No annealing	Average	1.09	21.41	62.33	14.51
	Highest	1.11	20.75	66.44	15.30
80 °C annealing	Average	1.11	21.68	65.95	15.86
	Highest	1.12	22.30	69.12	17.26
100 °C annealing	Average	1.12	21.92	66.24	16.23
	Highest	1.13	22.00	68.88	17.13
120 °C annealing	Average	1.12	21.32	67.55	16.20
	Highest	1.13	22.41	69.52	17.61
140 °C annealing	Average	1.09	21.26	62.37	14.48
	Highest	1.11	21.31	64.17	15.18

The statistical distribution graphs of the salt-treated solar cells with different annealing temperatures are given in Figure 3.7. Cells that were annealed at 100 °C and 120 °C displayed narrower statistical distribution and higher V_{OC} values.

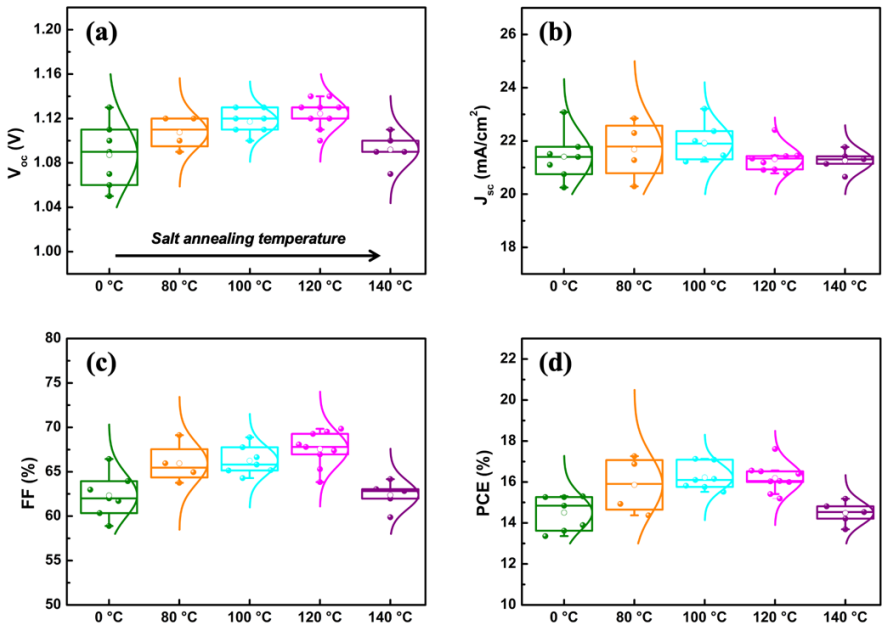

Figure 3.7. (a) V_{OC}, (b) J_{SC}, (c) FF, and (d) PCE statistics of PSCs with different salt annealing temperatures

J-V curves of the best-performing devices are plotted in Figure 3.8. The highest efficiencies were obtained as 17.13% (V_{OC} = 1.13 V, J_{SC} = 22.00 mA/cm^2, FF = 68.88%) for the device with the salt annealing temperature of 100 °C, and 17.61% (V_{OC} = 1.13 V, J_{SC} = 22.41 mA/cm^2, FF = 69.52%) for the device with the salt annealing temperature of 120 °C. Using these two annealing temperatures resulted in very similar device performances, hence, 100 °C was chosen as the optimum salt annealing temperature and used in the following experiments due to feasibility.

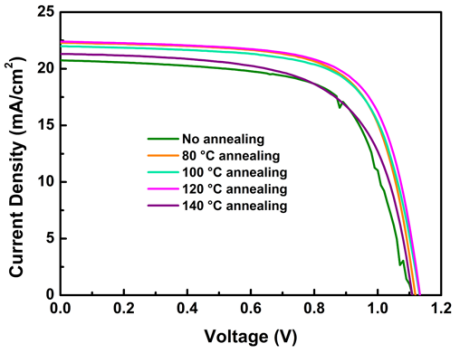

Figure 3.8. J-V curves of the best-performing devices with different salt annealing temperatures

3.2 Optimization of 3,5-MeO-PEAI

3,5-MeO-PEAI salt optimization was done systematically. Similar to the optimization of 2,6-MeO-PEAI, optimum concentration of the salt was chosen at first, followed by the optimization of spin rate for the salt coating step.

3.2.1 Concentration Optimization

With the aim of deciding the ideal concentration of salt, 1 mg, 2 mg, 3 mg and 4 mg of 3,5-MeO-PEAI salt was dissolved in IPA and coated with a spin rate of 3000 rpm on top of the perovskite layer, whereas no salt layer was included in the reference cells. The cells with 4 mg/mL of 3,5-MeO-PEAI performed the best in terms of both average and the highest PV parameters, as listed in Table 3.4. Below 3 mg/mL of salt concentration, PCE values of the salt-treated cells were highly similar to that of the reference cells. The cells with 4 mg/mL of salt concentration outperformed the other cells, owing to their superior V_{OC} values.

Table 3.4. Photovoltaic parameters of PSCs with different concentrations of 3,5-MeO-PEAI

Devices		V_{OC} (V)	J_{SC} (mA/cm^2)	FF (%)	PCE (%)
Reference	Average	1.10	22.02	71.53	17.38
	Highest	1.11	22.87	73.82	18.74
1 mg/mL	Average	1.09	22.00	74.71	17.93
	Highest	1.09	22.65	75.72	18.70
2 mg/mL	Average	1.07	22.01	74.75	17.57
	Highest	1.07	23.09	75.75	18.71
3 mg/mL	Average	1.10	22.06	73.83	17.86
	Highest	1.12	22.69	74.41	18.91
4 mg/mL	Average	1.13	22.26	72.60	18.27
	Highest	1.14	23.25	73.44	19.47

The statistical distribution graphs of the reference and salt-treated solar cells are presented in Figure 3.9. These graphs also supported the V_{OC} and PCE enhancement upon the treatment with 4 mg/mL of salt.

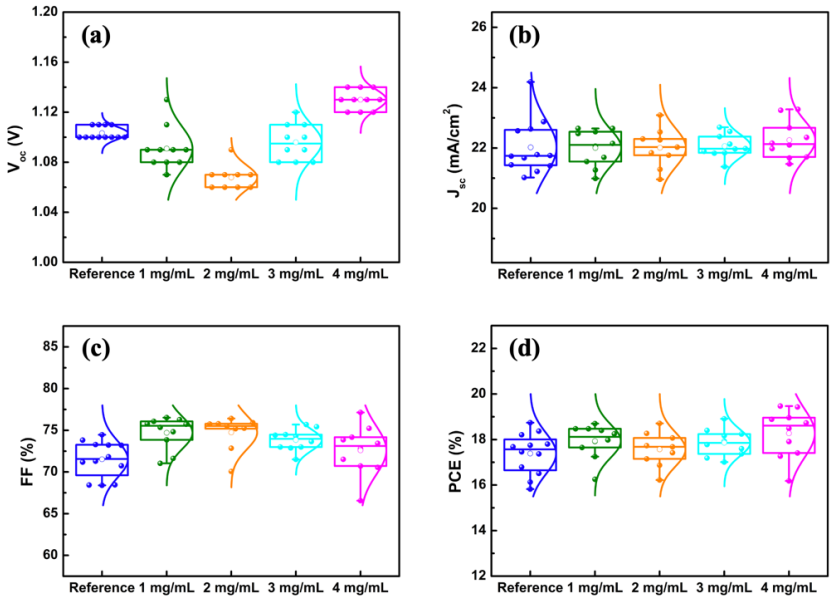

Figure 3.9. (a) V_{OC}, (b) J_{SC}, (c) FF, and (d) PCE statistics of PSCs with different concentrations of 3,5-MeO-PEAI

J-V curves of the best-performing devices are shown in Figure 3.10. The highest efficiencies were obtained as 18.74% (V_{OC} = 1.11 V, J_{SC} = 22.87 mA/cm^2, FF = 73.82%) for the reference device, and 19.47% (V_{OC} = 1.14 V, J_{SC} = 23.25 mA/cm^2, FF = 73.44%) for the device with 4 mg/mL of salt concentration. 4 mg/mL was chosen as the optimum salt concentration and used in the following experiments.

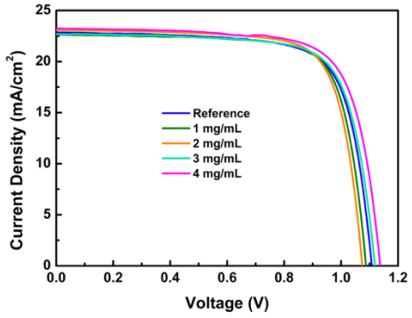

Figure 3.10. J-V curves of the best-performing devices with different concentrations of 3,5-MeO-PEAI

3.2.2 Spin Rate Optimization

For the spin rate optimization of the salt coating step, 3,5-MeO-PEAI dissolved in IPA was coated with a spin rate of 500, 1000, 2000, 3000 and 4000 rpm on top of the perovskite layer, whereas the reference cells did not contain the salt layer. The salt-treated cells coated with 500 and 1000 rpm exhibited superior V_{OC} values compared to the other cells, which can be seen in Table 3.5. On the other hand, FF values of the cells with the salt coating spin rate of 500 rpm were lower, most probably owing to the fact that coating with this spin rate created too thick of a salt layer. The cells with the salt coating spin rate of 1000 rpm demonstrated enhanced V_{OC} values without comprimising from FF values, which resulted in the best average and the highest PCE values.

Table 3.5. Photovoltaic parameters of PSCs with different spin rates of 3,5-MeO-PEAI

Devices		V_{OC} (V)	J_{SC} (mA/cm^2)	FF (%)	PCE (%)
Reference	Average	1.10	22.02	71.53	17.38
	Highest	1.11	22.87	73.82	18.74
500 rpm	Average	1.13	21.83	70.69	17.45
	Highest	1.14	22.46	72.39	18.54
1000 rpm	Average	1.13	22.55	73.91	18.79
	Highest	1.13	22.94	74.87	19.41
2000 rpm	Average	1.10	21.58	74.43	17.75
	Highest	1.12	22.36	75.22	18.84
3000 rpm	Average	1.10	21.93	74.83	18.05
	Highest	1.10	23.38	74.48	19.16
4000 rpm	Average	1.11	21.60	72.97	17.49
	Highest	1.11	22.15	72.37	17.79

The statistical distribution graphs of the reference and salt-treated solar cells are demonstrated in Figure 3.11. Enhanced V_{OC} and PCE as well as the narrower distribution for the cells with the salt coating spin rate of 1000 rpm were seen clearly.

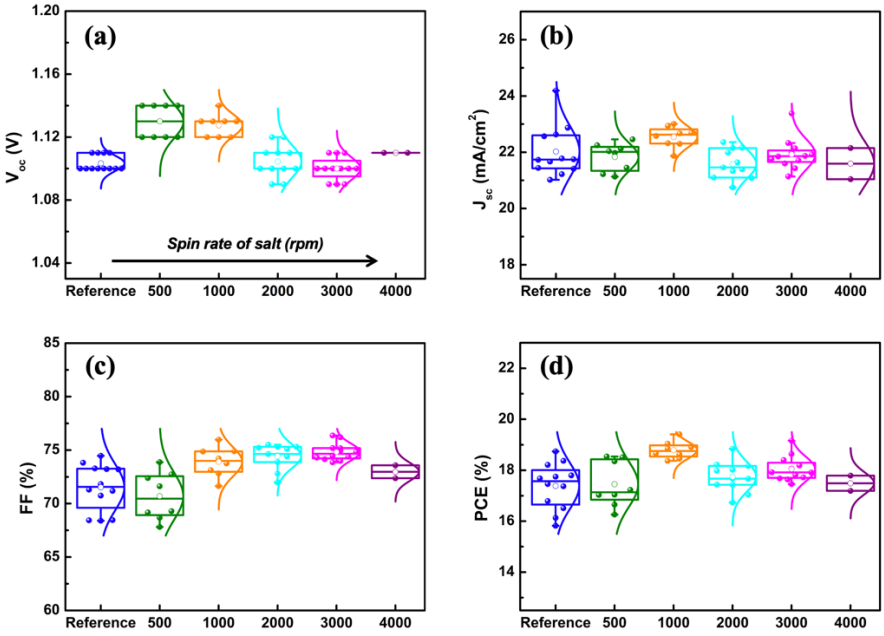

Figure 3.11. (a) V_{OC}, (b) J_{SC}, (c) FF, and (d) PCE statistics of PSCs with different spin rates of 3,5-MeO-PEAI

J-V curves of the best-performing devices are shown in Figure 3.12. The highest efficiencies were obtained as 18.74% (V_{OC} = 1.11 V, J_{SC} = 22.87 mA/cm^2, FF = 73.82%) for the reference device, and 19.41% (V_{OC} = 1.13 V, J_{SC} = 22.94 mA/cm^2, FF = 74.87%) for the salt-treated device coated with 1000 rpm. 1000 rpm was chosen as the optimum spin rate for salt coating step and used in the following experiments.

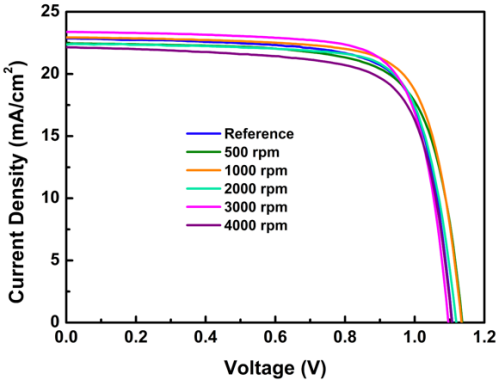

Figure 3.12. J-V curves of the best-performing devices with different spin rates of 3,5-MeO-PEAI

3.2.2.1 Grazing Incidence X-Ray Diffraction

Samples were fabricated for grazing incidence X-ray diffraction (GIXRD) measurement in the structure of FTO/SnO_2/Perovskite/3,5-MeO-PEAI. 3,5-MeO-PEAI salt was coated with a spin rate of 500, 1000, 2000, 3000 and 4000 rpm on top of the perovskite layer, whereas the reference sample did not contain the salt layer. The GIXRD measurement result is demonstrated in Figure 3.13. Upon salt addition, a small peak occurred at around 7°, which could be attributed to the possible 2D layer formation. In addition, new peaks were observed at around 4.8° and 3.8° for the salt-treated samples coated with 500 and 1000 rpm, whereas these new peaks were not observed for the other salt-treated samples. The occurrence of these peaks for the samples with thicker salt layer indicated that these peaks were related with the salt itself. GIXRD peaks were investigated in more detail under Chapter 3 in Section 3.3.2.1.1.

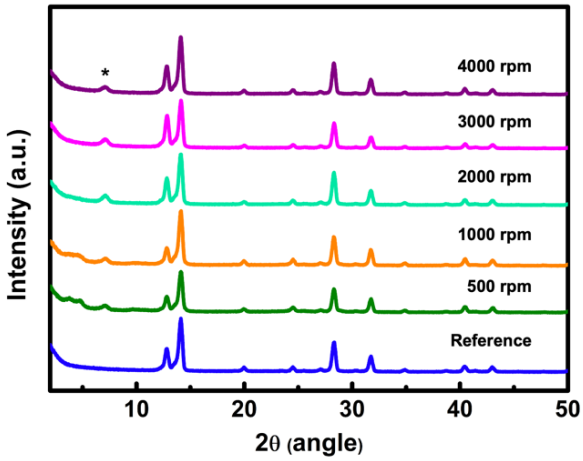

Figure 3.13. GIXRD patterns of the reference sample and samples with different spin rates of 3,5-MeO-PEAI; * represents the new peak at around 7° upon salt addition

3.3 Comparison of Novel Cations and Annealing Study

The experimental studies with 2,6-MeO-PEAI demonstrated that the optimum concentration and spin rate of this salt was 2 mg/mL and 1500 rpm, respectively. On the other hand, for 3,5-MeO-PEAI, the optimum concentration and spin rate were found as 4 mg/mL and 1000 rpm, respectively. After deciding these parameters, solar cells were fabricated using the optimum values with the aim of comparing the performances of the two salts. Furthermore, in the same study, the salt annealing effect was also investigated. Average and the highest device performances of this study are listed in Table 3.6. In the table and the following figures, '2,6' and '3,5' were used as short for 2,6-MeO-PEAI and 3,5-MeO-PEAI salts, respectively. Also, with annealing (or a+ in short) term was used meaning that salt was subjected to thermal annealing at 100 °C, and without annealing (or a- in short) term was used meaning that salt was not annealed. The cells with annealed 2,6-MeO-PEAI performed the best due to a slight enhancement of V_{OC} and FF compared to the reference cells. The cells with annealed 3,5-MeO-PEAI, for which 2D layer formation was observed as shown in Section 3.3.2.1.1, exhibited lower J_{SC} values than the other cells. This could arise from the fact that the insulating nature of 2D perovskites limits the charge transport and thus, reduces the J_{SC} values.[111] It should be noted that even though the performance of the cells with 3,5-MeO-PEAI did not exceed that of the reference cells, 3,5-MeO-PEAI treatment substantially improved V_{OC}. Moreover, salt annealing improved the performance for the cells treated with 2,6-MeO-PEAI, whereas it resulted in a poorer performance for the cells treated with 3,5-MeO-PEAI.

Table 3.6. Photovoltaic parameters of the reference and salt-treated PSCs with or without salt annealing

Devices		V_{OC} (V)	J_{SC} (mA/cm^2)	FF (%)	PCE (%)
Reference	Average	1.09	21.99	71.93	17.21
	Highest	1.09	23.11	72.02	18.14
2,6 with annealing	Average	1.10	21.81	72.12	17.38
	Highest	1.11	23.46	73.55	19.15
2,6 without annealing	Average	1.09	21.58	73.41	17.31
	Highest	1.10	22.14	75.05	18.28
3,5 with annealing	Average	1.14	20.99	66.99	16.03
	Highest	1.13	21.91	68.63	16.99
3,5 without annealing	Average	1.13	21.31	70.18	16.86
	Highest	1.13	21.74	72.82	17.89

The statistical distribution graphs of the reference and salt-treated solar cells are given in Figure 3.14. In these graphs, slight enhancement in V_{OC} and FF of the cells with annealed 2,6-MeO-PEAI was observed. Additionally, cells with annealed 3,5-MeO-PEAI displayed the highest V_{OC}, however their FF values were poor, which resulted in a lower efficiency.

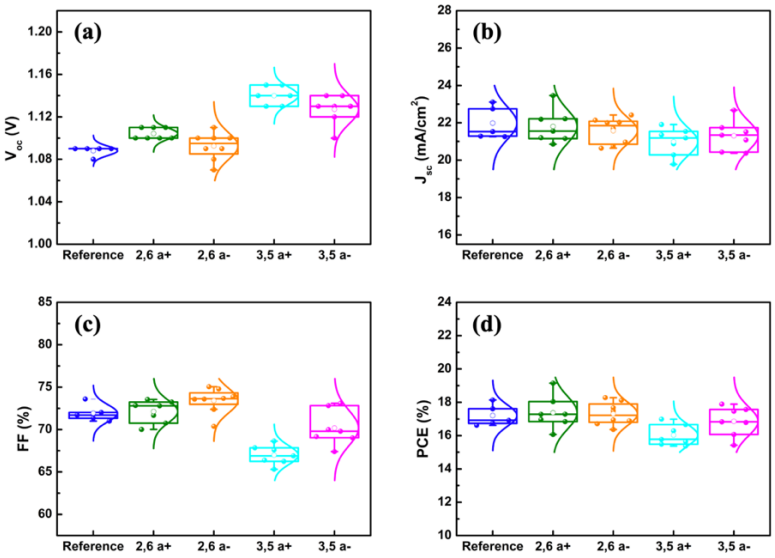

Figure 3.14. (a) V_{OC}, (b) J_{SC}, (c) FF, and (d) PCE statistics of the reference and salt-treated PSCs with or without salt annealing

J-V curves of the best-performing devices are shown in Figure 3.15. The highest efficiencies were obtained as 18.14% (V_{OC} = 1.09 V, J_{SC} = 23.11 mA/cm^2, FF = 72.02%) for the reference device, 17.89% (V_{OC} = 1.13 V, J_{SC} = 21.74 mA/cm^2, FF = 72.82%) for the device with non-annealed 3,5-MeO-PEAI, and 19.15% (V_{OC} = 1.11 V, J_{SC} = 23.46 mA/cm^2, FF = 73.55%) for the device with annealed 2,6-MeO-PEAI.

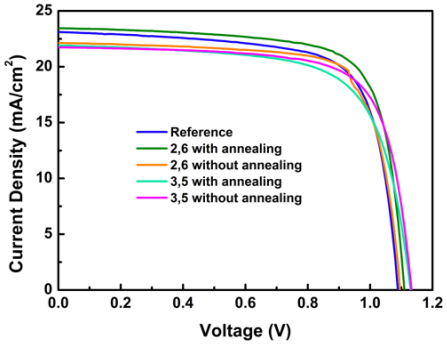

Figure 3.15. J-V curves of the best-performing devices of the reference and salt-treated PSCs with or without salt annealing

Hysteresis phenomena was seen for all the devices, as shown in Figure 3.16, where the solid curves indicated reverse scan and the dashed curves indicated forward scan in J-V measurements. From Equation 1.8, hysteresis index was calculated as 0.24 for the reference device, whereas it was calculated as 0.15, 0.16, 0.29, and 0.15 for the devices with annealed 2,6-MeO-PEAI, non-annealed 2,6-MeO-PEAI, annealed 3,5-MeO-PEAI, and non-annealed 3,5-MeO-PEAI, respectively.

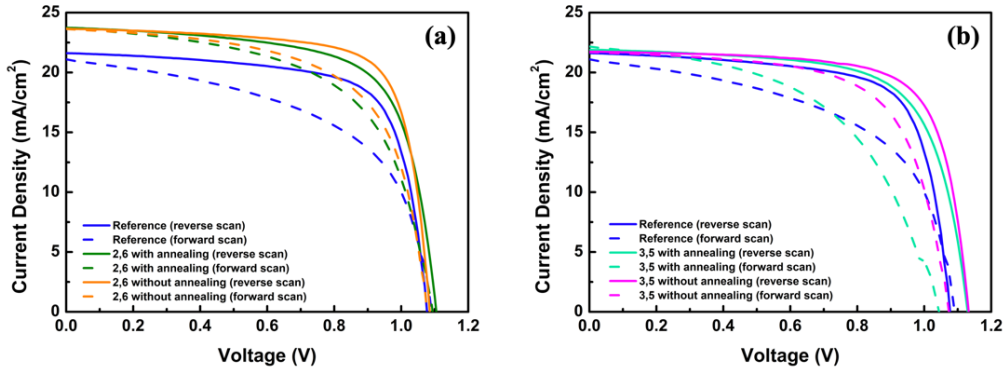

Figure 3.16. J-V curves obtained by reverse and forward scans demonstrating hysteresis for the reference and (a) 2,6-MeO-PEAI-treated, (b) 3,5-MeO-PEAI-treated devices with or without salt annealing

3.3.1 Device Characterization

This section includes the results of the electrical measurements, external quantum efficiency (EQE) and impedance spectroscopy, of the salt comparison and annealing study. For these characterizations, cells that were fabricated for the salt comparison and annealing study were used.

3.3.1.1 External Quantum Efficiency

EQE measurements were performed to obtain the integrated J_{SC} values. First, J-V measurement was conducted, followed by EQE measurement. J_{SC} values obtained from J-V and EQE measurements and EQE spectra are shown in Table 3.7 and Figure 3.17, respectively. EQE measurement demonstrated that the best J_{SC} belonged to the cell with non-annealed 3,5-MeO-PEAI, followed by the cell with non-annealed 2,6-MeO-PEAI. All the salt-treated devices exhibited higher J_{SC} values than the reference device. It should be noted that since the reference device quickly degraded, the J_{SC} values obtained from J-V was lower than the previous measurement, which was shown in Table 3.6. Moreover, a slight decrease in J_{SC} obtained from EQE was observed for most of the devices, however it was highly significant for the reference device. This could stem from the possibility that the light stability of the reference device was quite poor.

Table 3.7. J_{SC} values obtained from J-V and EQE measurements

Devices	J_{SC} (mA/cm^2) from J-V	J_{SC} (mA/cm^2) from EQE
Reference	21.37	17.90
2,6 with annealing	22.81	20.52
2,6 without annealing	23.44	22.46
3,5 with annealing	21.77	20.80
3,5 without annealing	23.08	23.15

Since photons with shorter wavelengths have higher energy, when these photons are incident on a cell, they can generate carriers immediately. On the other hand, photons with longer wavelengths have lower energy and longer penetration depth. Therefore, EQE graph allows us to determine the carrier recombination near the front (TCO, ETL) and rear (HTL, metal) interfaces from the short-wavelength region and the long-wavelength region, respectively.[122] From Figure 3.17, the reference device was observed to experience more losses, which were mainly in the long-wavelength region. Thus, for the reference device, the reduction of EQE spectrum at long wavelengths could be explained by having more carrier recombination occurring at the perovskite/HTL interface.

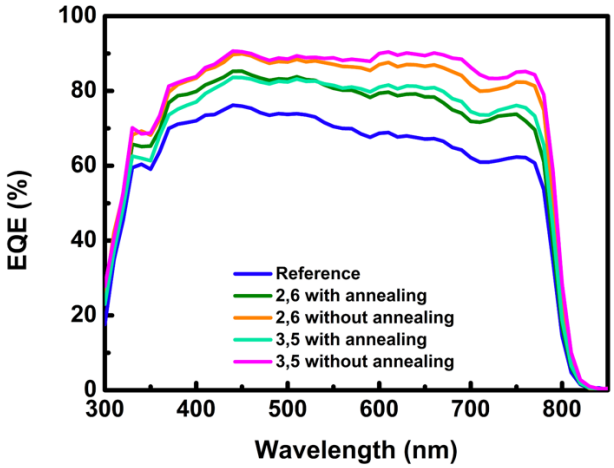

Figure 3.17. EQE spectra of the reference and salt-treated devices with or without salt annealing

Moreover, any light below the band gap energy will not be absorbed by the cells. After the wavelength that corresponds to the band gap, incoming light will not be absorbed, thereby EQE will be zero.[116] In Figure 3.17, EQE signal dropped to zero at around 830 nm, from which a band gap of ~1.49 eV could be inferred by the Equation 2.3. This is consistent with the band gap of perovskites in the literature, which is around 1.48-1.62 eV.[123]

3.3.1.2 Impedance Spectroscopy

Impedance spectroscopy measurements were conducted to investigate recombination dynamics inside the device. The measurements were performed under the illumination of 0.1 suns and open-circuit condition. Under these conditions, charge carrier generation was suppressed by recombination, and thus, there is no net carrier transport between the perovskite layer and interfaces. Thus, the recombination processes of PSCs can be inferred from the impedance spectra. Impedance spectra of the reference and salt-treated devices were displayed via Nyquist plots, as shown in Figure 3.18. The high-frequency semi-circle is generally attributed to the recombination resistance and the geometrical capacitance.[124] Therefore, the increase of the high-frequency semi-circle upon addition of the salt layer indicated less recombination inside the device since recombination resistance increased. The biggest semi-circle belonged to the device with annealed 3,5-MeO-PEAI, followed by the device with non-annealed 3,5-MeO-PEAI. These devices also demonstrated the highest V_{OC} values, as shown in Table 3.6. Impedance spectroscopy results were consistent with J-V measurement results, as expected since less surface recombination would lead to higher V_{OC} values.

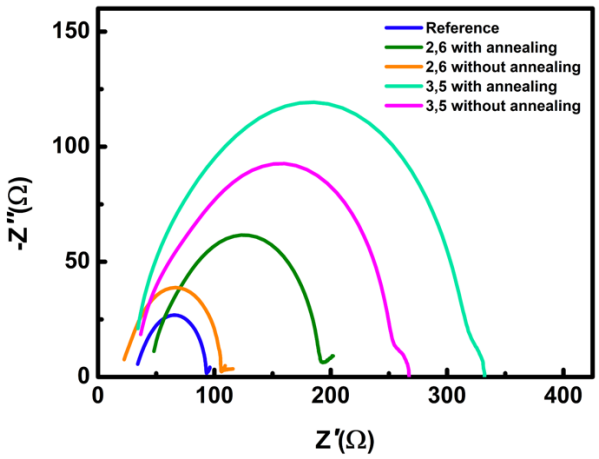

Figure 3.18. Nyquist plots of the reference and salt-treated PSCs obtained from the impedance measurement

3.3.2 Film Characterization

This section includes grazing incidence X-ray diffraction (GIXRD), photoluminescence (PL), and ultraviolet photoelectron spectroscopy (UPS) measurement results of the salt comparison and annealing study. For these characterizations, thin films were fabricated with the same fabrication procedure, except for the thermal evaporation step.

3.3.2.1 Grazing Incidence X-Ray Diffraction

Samples were fabricated for GIXRD measurement in the structure of FTO/SnO_2/Perovskite/Salt. Either 2,6-MeO-PEAI or 3,5-MeO-PEAI salt was coated on top of the perovskite layer, whereas the reference samples did not contain the salt layer. GIXRD measurement results are demonstrated in Figure 3.19. For both salts, a new peak occurred between 5-10° upon salt annealing which could be attributed to the possible 2D layer formation.[121] If the new peaks indeed indicated 2D perovskite, this would infer that salts created 2D perovskite only when they were annealed and did not create a 2D layer when they were not subjected to annealing. To check whether the new peaks indicated 2D layer or not, 2D-only and quasi-2D perovskite thin films were fabricated; which is explained in Section 3.3.2.1.1.

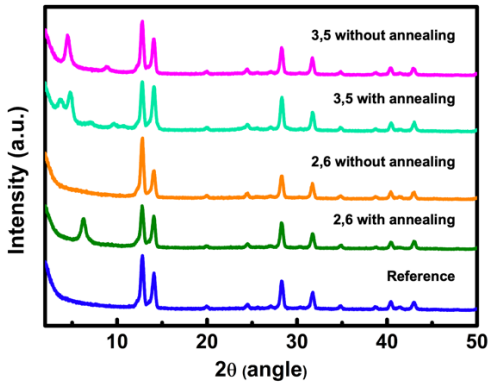

Figure 3.19. GIXRD patterns of the reference and salt-treated samples with or without annealing

3.3.2.1.1 GIXRD Analysis of 2D and Quasi-2D Films

Solutions for 2D perovskite (n = 1) film were prepared by dissolving salt (either 2,6-MeO-PEAI or 3,5-MeO-PEAI) and PbI_2 (2:1) in DMF:DMSO (15:5) (v:v) mixture. Precursor solutions for MAI incorporated quasi-2D perovskite (n = 2) were prepared by dissolving salt, MAI, PbI_2 (2:1:2) in DMF:DMSO (15:5) (v:v) mixture. All solutions were coated onto FTO/SnO_2 substrates at 3000 rpm for 30 seconds and annealed at 100 °C for 10 minutes. Additionally, salt only films were fabricated by dissolving salt in IPA (2 mg/mL) and coating this solution on FTO substrates at 3000 rpm for 30 seconds, followed by annealing at 100 °C for 10 minutes.

GIXRD measurement results of the prepared films for both salts are shown in Figure 3.20. The diffraction peaks of PbI_2 and 3D perovskite were clearly observed as indicated in the figure.

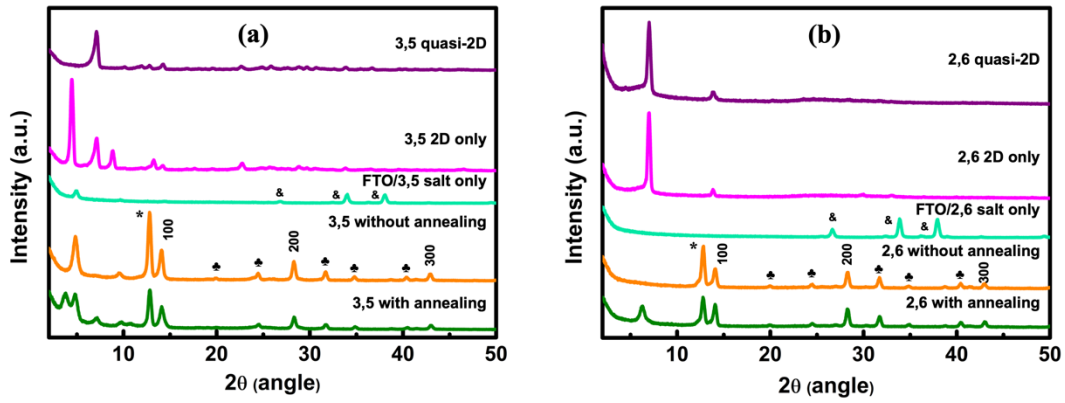

Figure 3.20. GIXRD patterns of films prepared with (a) 3,5-MeO-PEAI, and (b) 2,6-MeO-PEAI; *, ♣, and & represent diffraction peaks of PbI_2, 3D perovskite, and FTO, respectively

To investigate the low angle region and identify the possible 2D perovskite peaks, GIXRD patterns were scaled to the 2-10° region, as shown in Figure 3.21. For 3,5-MeO-PEAI, the peak at 7.11° was identified as the 2D perovskite peak, which was indicated with the dashed line in Figure 3.21a. Since the sample with annealed 3,5-MeO-PEAI had the same peak, it was demonstrated that 3,5-MeO-PEAI created 2D perovskite upon annealing. Annealing-dependent 2D layer formation was consistent

with the literature.[87,115] Additionally, the quasi-2D sample also had a peak at 7.11°, which confirmed the formation of quasi-2D perovskite with the incorporation of MA^+ ions. Moreover, it was observed that the salt only sample (FTO/3,5-MeO-PEAI) had a peak at 4.88°, shown with the dotted line in Figure 3.21a, which had to be related with the salt itself. This peak appeared in all samples, except for the quasi-2D sample, and slightly shifted to the left (4.46°) for the 2D only sample. This peak was considered to originate from the crystal structure of 3,5-MeO-PEAI. It was also noticed that the sample with annealed 3,5-MeO-PEAI had a peak splitting, which could take place due to the phase transformation.[125] For 2,6-MeO-PEAI, the peak at 7° was identified as the 2D perovskite peak, which was indicated with the dashed line in Figure 3.21b. The quasi-2D sample also had the same peak, which confirmed the formation of quasi-2D perovskite with the incorporation of MA^+ ions. However, the 2D peak was not seen for the sample with annealed 2,6-MeO-PEAI. Instead, the sample with annealed 2,6-MeO-PEAI had a peak at 6.27°, shown with the dotted line in Figure 3.21b. Considering the variation between these peaks, it was concluded that 2,6-MeO-PEAI salt did not create a pure 2D perovskite. Also, the peak at 6.27° could not be related with the salt itself due to the lack of this peak in the salt only sample. This peak was thought to be attributed to the possible formation of higher dimensional (n > 2) perovskite layer.

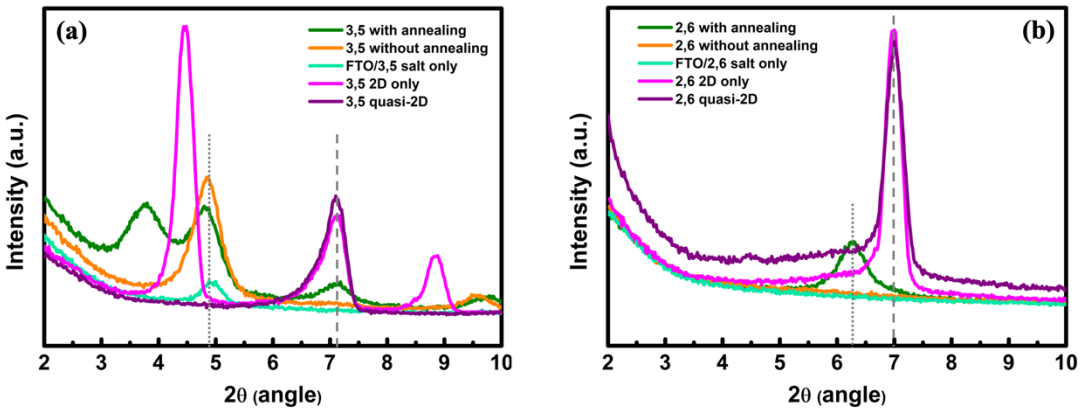

Figure 3.21. Scaled GIXRD patterns of films prepared with (a) 3,5-MeO-PEAI, and (b) 2,6-MeO-PEAI; dashed lines represent the diffraction peak of 2D perovskite

It was evident that the distance of two methoxy groups with respect to the ethylammonium group affected the interaction between the novel cations and perovskite. The cations with different dipole moments led to varying electron density on the aromatic ring, which might be the reason for the difference in cation-perovskite interaction.[109] Nevertheless, this interaction depending on the structural change of the cations remained unclear and required for further investigation.

3.3.2.2 Photoluminescence

Samples were fabricated for photoluminescence (PL) measurement in the structure of Glass/Perovskite/Salt. Either 2,6-MeO-PEAI or 3,5-MeO-PEAI salt was coated on top of the perovskite layer, whereas the reference samples did not contain the salt layer. PL measurement was performed to investigate the nonradiative recombination process. Upon treatment with annealed 2,6-MeO-PEAI, a significant increase in the PL intensity was observed, as shown in Figure 3.22. PL intensity increase is generally related with reduced trap density and nonradiative recombination, thus better passivation.[126] It was concluded that the treatment with annealed 2,6-MeO-PEAI passivated the surface defects and reduced the nonradiative recombination, which was consistent with J-V results presented in Table 3.6, where the sample with annealed 2,6-MeO-PEAI performed the best by enhancing V_{OC} and FF slightly. The sample with non-annealed 3,5-MeO-PEAI had also higher PL intensity than the reference. PL intensities of the reference sample and the sample with annealed 3,5-MeO-PEAI were very similar. PL intensities of the samples treated with 3,5-MeO-PEAI were expected to be much higher than that of the reference sample, due to their superior V_{OC} values. However, the presented results were different than expected, which could stem from a possible measurement error, and requires further investigation. On the other hand, a decrease in the PL intensity was observed for the sample with non-annealed 2,6-MeO-PEAI. V_{OC} values of this sample was observed to be very similar to the reference sample in J-V measurements. PL intensity decrease is generally related with better charge extraction or higher surface recombination

rate.[89,117] PL quenching observed in this sample could be associated with increased surface recombination velocity and better hole transport, which resulted in enhanced FF values, as presented in Table 3.6.

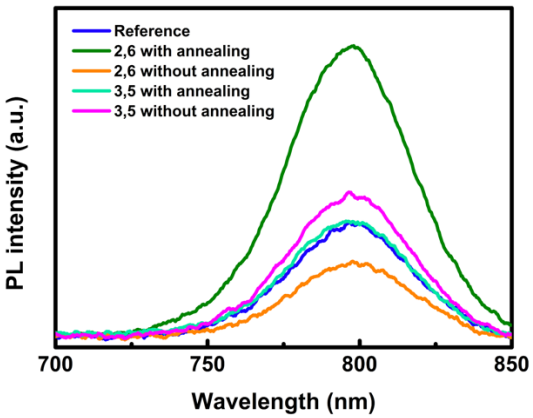

Figure 3.22. PL spectra of the reference and salt-treated samples with or without annealing

3.3.2.3 Ultraviolet Photoelectron Spectroscopy

Samples were fabricated for ultraviolet photoelectron spectroscopy (UPS) measurement in the structure of FTO/SnO_2/Perovskite/Salt. Either 2,6-MeO-PEAI or 3,5-MeO-PEAI salt was coated on top of the perovskite layer, whereas the reference samples did not contain the salt layer. UPS measurement was performed to investigate the band alignment and determine valence band maximum energy levels and the work function. UPS spectra of the reference and salt-treated samples are shown in Figure 3.23. For the reference sample, E_0 and E_{VBM} were found as 10.31 and -5.19 eV, respectively, and ionization energy was calculated as 5.72 eV from the Equations 2.5 and 2.6. For the sample with annealed 2,6-MeO-PEAI, E_0 and E_{VBM} were found as 10.63 and -4.81 eV, respectively, and ionization energy was calculated as 5.78 eV. For the sample with annealed 3,5-MeO-PEAI, E_0 and E_{VBM} were found as 10.00 and -5.31 eV, respectively, and ionization energy was calculated as 5.91 eV.

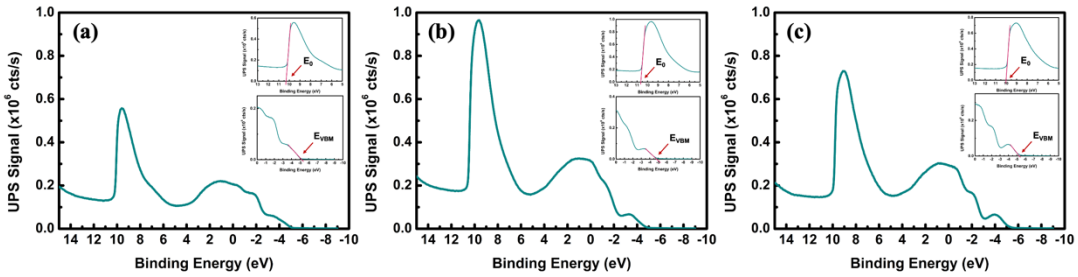

Figure 3.23. UPS spectra of the (a) reference, (b) 2,6-MeO-PEAI-treated, and (c) 3,5-MeO-PEAI-treated samples; inset figures show E_0 and E_{VBM} calculations

The energy band diagram of the PSC layers is illustrated in Figure 3.24, which demonstrates band alignment of the bare and salt-treated perovskite with the transport layers. Since the ionization energies of the reference and 2,6-MeO-PEAI-treated samples were very similar, band alignment between the 2,6-MeO-PEAI-treated perovskite and Spiro-OMeTAD was suitable. However, 3,5-MeO-PEAI had a higher ionization energy, which resulted in an unfavorable band alignment and poorer hole transport. This might be the reason for the lower FF values of the samples treated with 3,5-MeO-PEAI that was observed in J-V measurements.

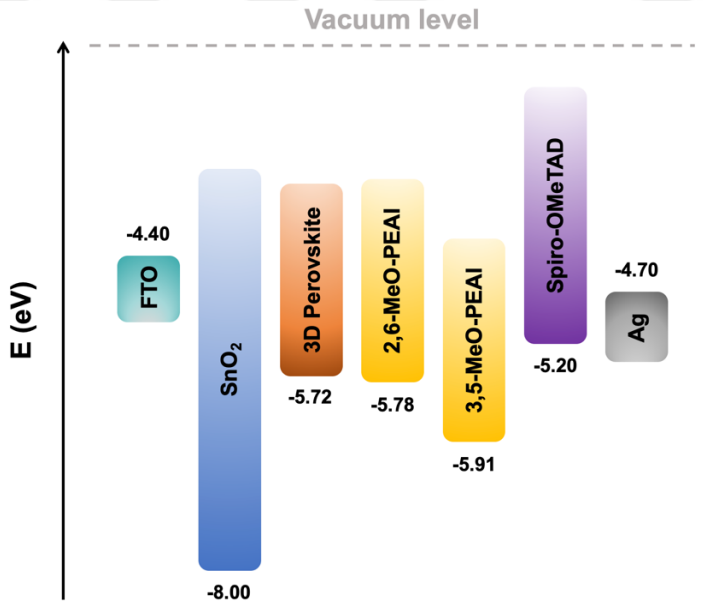

Figure 3.24. Schematic representation of the energy level diagram of the PSC layers

3.4 Stability Studies of Perovskite Solar Cells

The aim of perovskite research was not only to increase the efficiency but also improve the stability. Therefore, the stability of the unencapsulated PSCs was investigated. This section includes light stability results, which were achieved by maximum power point tracking (MPPT) measurement, long-term stability results, and moisture stability results, which were investigated by contact angle measurement.

3.4.1 Light Stability

For the light stability test, maximum power point tracking (MPPT) measurement was conducted in the J-V system. During the MPPT measurement, devices were in the laboratory (in ambient air with RH of ~20-40%, at RT) under a constant illumination of 1 sun. The device with 2,6-MeO-PEAI displayed the highest PCE value, whereas the reference device displayed the lowest PCE value, as shown in Figure 3.25. All devices exhibited quite stable PCE outputs for 850 seconds. Thereafter, the output of the reference device started to fluctuate and did not exhibit a proper PCE output. However, this problem was not observed for the salt-treated devices. Small fluctuations between 1000-1500 seconds occurred for the device treated with 3,5-MeO-PEAI, which then diminished and turned to the stable PCE output again. This might result from contact problems of the crocodile clips. Additionally, the maximum PCE output displayed by the reference cell, the cell with 2,6-MeO-PEAI, and the cell with 3,5-MeO-PEAI was 17.55%, 21.60%, and 19.46%, respectively. When these values were compared with the PCE outputs at the end of the measurement, a PCE drop of 3.70%, 1.94%, and 2.88% was calculated for the reference cell, the cell with 2,6-MeO-PEAI, and the cell with 3,5-MeO-PEAI, respectively. Therefore, it was concluded that salt-treatment enhanced the light stability of the solar cells.

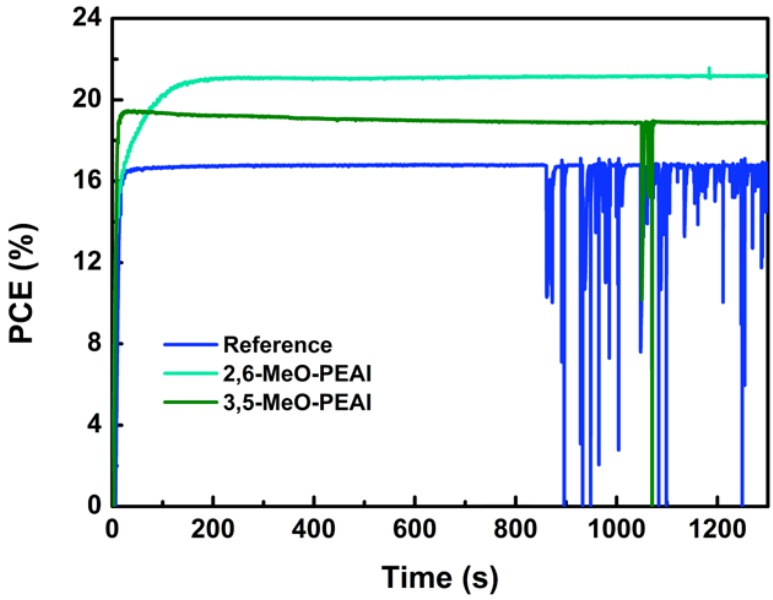

Figure 3.25. Maximum power point tracking of the reference and salt-treated PSCs

3.4.2 Long-Term Stability

Long-term environmental stability of the solar cells was determined by conducting current density-voltage measurements of the cells in the J-V system regularly. Devices were kept in the desiccator (at RT, in the dark) that had a relative humidity below 15%. Devices with salt treatment exhibited superior stability compared to the reference device, as shown in Figure 3.26. The cell with 3,5-MeO-PEAI and 2,6-MeO-PEAI maintained 94% and 93% of the initial PCE, respectively, whereas the reference cell maintained 77% of the initial PCE after six weeks from the fabrication.

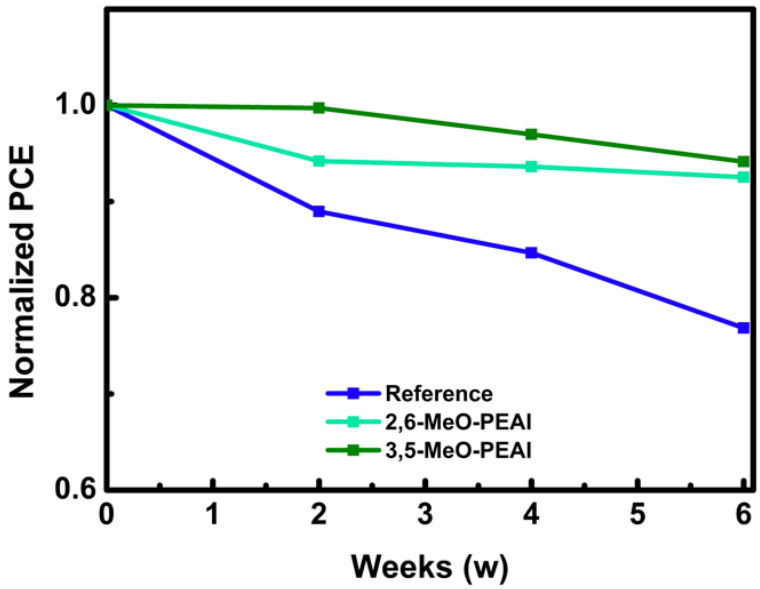

Figure 3.26. Normalized PCEs of the reference and salt-treated PSCs, kept in the desiccator with RH of < 15%, at RT, in the dark

3.4.3 Moisture Stability

Moisture stability was assessed with contact angle measurement using water. Samples were fabricated for the measurement in the structure of FTO/SnO_2/Perovskite/Salt. Either 2,6-MeO-PEAI or 3,5-MeO-PEAI salt was coated on top of the perovskite layer, whereas the reference samples did not contain the salt layer. Contact angle measurement was conducted to investigate the effect of salt addition on the hydrophobicity of the 3D perovskite. It was known that the larger the contact angle, the more hydrophobic the film surface was. As shown in Figure 3.27, hydrophobicity increased for the samples with annealed salts, however, it decreased for the samples without salt annealing.

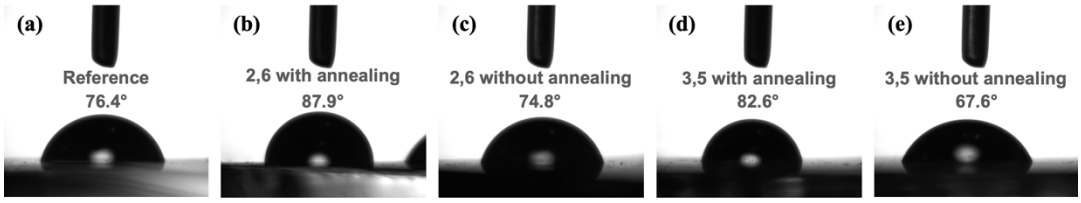

Figure 3.27. Contact angle images of the (a) reference sample, and samples treated with (b) annealed 2,6-MeO-PEAI, (c) non-annealed 2,6-MeO-PEAI, (d) annealed 3,5-MeO-PEAI, (e) non-annealed 3,5-MeO-PEAI

Since the samples with annealed salts created 2D or quasi-2D layers on top of the 3D perovskite, as shown in GIXRD measurements, these layers could act as moisture resistant layers, which could suppress the cell degradation caused by humidity, and give rise to higher contact angle results. The enhancement in the contact angle could originate from the hydrophobic nature of the PEAI part of the salts.[127]

CHAPTER 4

CONCLUSION

In this study, two novel cations, that are 2,6-methoxy-phenylethyl ammonium iodide (2,6-MeO-PEAI) and 3,5-methoxy-phenylethyl ammonium iodide (3,5-MeO-PEAI) were used on top of $(FAPbI_3)_{1-x}(MAPbBr_3)_x$ (FAMA) perovskite, as a result, an increase in open-circuit voltage (V_{OC}) and enhancement of stability was observed. 2,6-MeO-PEAI salt did not form a pure 2D perovskite, whereas 3,5-MeO-PEAI salt created a 2D layer upon annealing, as shown with grazing incidence X-ray diffraction measurements. To investigate the increase in V_{OC}, photoluminescence and impedance spectroscopy measurements were conducted, which revealed that nonradiative recombination was reduced upon salt treatment. The highest increase in V_{OC} was achieved with the addition of 3,5-MeO-PEAI salt, exhibiting a V_{OC} of 1.14 eV. The cells with 2,6-MeO-PEAI salt demonstrated the best overall performance, by increasing the PCE from 18.14% for the reference to 19.15%. Furthermore, the light stability, long-term stability as well as the moisture stability of the devices with the salt treatment enhanced greatly. The cell with 3,5-MeO-PEAI and 2,6-MeO-PEAI maintained 94% and 93% of the initial PCE, respectively, whereas the reference cell maintained 77% of the initial PCE after six weeks from the fabrication. This study have shown the importance of interface engineering using novel organic cations, that not only passivates the defects of the perovskite film and thus, minimizes the nonradiative recombination, but also allows to fabricate more stable perovskite solar cells.

REFERENCES

1. Marques Lameirinhas, R., Torres, J. & de Melo Cunha, J. A photovoltaic technology review: history, fundamentals and applications. *Energies* **15**, 1823 (2022).
2. Jäger, K.-D., Isabella, O., Smets, A. H. M., Van Swaaij, R. A. C. M. M. & Zeman, M. *Solar energy: fundamentals, technology and systems*. *UIT Cambridge* (2016).
3. Liu, J., Yao, M. & Shen, L. Third generation photovoltaic cells based on photonic crystals. *J. Mater. Chem. C* **7**, 3121–3145 (2019).
4. Chen, Q. *et al.* Under the spotlight: The organic-inorganic hybrid halide perovskite for optoelectronic applications. *Nano Today* **10**, 355–396 (2015).
5. Li, S. *et al.* Metal halide perovskite single crystals: From growth process to application. *Crystals* **8**, 220 (2018).
6. Green, M. A., Ho-Baillie, A. & Snaith, H. J. The emergence of perovskite solar cells. *Nat. Photonics* **8**, 506–514 (2014).
7. Travis, W., Glover, E. N. K., Bronstein, H., Scanlon, D. O. & Palgrave, R. G. On the application of the tolerance factor to inorganic and hybrid halide perovskites: A revised system. *Chem. Sci.* **7**, 4548–4556 (2016).
8. Gao, P., Grätzel, M. & Nazeeruddin, M. K. Organohalide lead perovskites for photovoltaic applications. *Energy Environ. Sci.* **7**, 2448–2463 (2014).
9. Xing, G. *et al.* Low-temperature solution-processed wavelength-tunable perovskites for lasing. *Nat. Mater.* **13**, 476–480 (2014).
10. Yu, J. C., Kim, D. Bin, Jung, E. D., Lee, B. R. & Song, M. H. High-performance perovskite light-emitting diodes via morphological control of perovskite films. *Nanoscale* **8**, 7036–7042 (2016).
11. Liu, A. *et al.* High-performance inorganic metal halide perovskite transistors. *Nat. Electron.* **5**, 78–83 (2022).
12. Yang, W. S. *et al.* Iodide management in formamidinium-lead-halide-based perovskite layers for efficient solar cells. *Science (80-.).* **356**, 1376–1379 (2017).
13. Kojima, A., Teshima, K., Shirai, Y. & Miyasaka, T. Organometal halide perovskites as visible-light sensitizers for photovoltaic cells. *J. Am. Chem. Soc.* **131**, 6050–6051 (2009).
14. Im, J.-H., Lee, C.-R., Lee, J.-W., Park, S.-W. & Park, N.-G. 6.5% efficient perovskite quantum-dot-sensitized solar cell. *Nanoscale* **3**, 4088 (2011).

15. Kim, H.-S. *et al.* Lead iodide perovskite sensitized all-solid-state submicron thin film mesoscopic solar cell with efficiency exceeding 9%. *Sci. Rep.* **2**, (2012).

16. NREL Efficiency Chart. https://www.nrel.gov/pv/assets/pdfs/cell-pv-eff-emergingpv-rev220630.pdf (2022).

17. Roy, P., Kumar Sinha, N., Tiwari, S. & Khare, A. A review on perovskite solar cells: Evolution of architecture, fabrication techniques, commercialization issues and status. *Sol. Energy* **198**, 665–688 (2020).

18. Jena, A. K., Kulkarni, A. & Miyasaka, T. Halide perovskite photovoltaics: Background, status, and future prospects. *Chem. Rev.* **119**, 3036–3103 (2019).

19. McDonald, C. *et al.* Nanostructured perovskite solar cells. *Nanomaterials* **9**, 1481 (2019).

20. Wang, K. *et al.* Novel inorganic electron transport layers for planar perovskite solar cells: Progress and prospective. *Nano Energy* **68**, 104289 (2020).

21. Lekesi, L. P., Koao, L. F., Motloung, S. V., Motaung, T. E. & Malevu, T. Developments on perovskite solar cells (PSCs): A critical review. *Appl. Sci.* **12**, 672 (2022).

22. Saliba, M. *et al.* How to make over 20% efficient perovskite solar cells in regular (n-i-p) and inverted (p-i-n) architectures. *Chem. Mater.* **30**, 4193–4201 (2018).

23. Cheng, M. *et al.* Charge-transport layer engineering in perovskite solar cells. *Sci. Bull.* **65**, 1237–1241 (2020).

24. Zheng, S. *et al.* Materials and structures for the electron transport layer of efficient and stable perovskite solar cells. *Sci. China Chem.* **62**, 800–809 (2019).

25. Mohamad Noh, M. F. *et al.* The architecture of the electron transport layer for a perovskite solar cell. *J. Mater. Chem. C* **6**, 682–712 (2018).

26. Zhang, W. *et al.* Recent advance in solution-processed organic interlayers for high-performance planar perovskite solar cells. *Adv. Sci.* **5**, (2018).

27. Wang, Y., Yue, Y., Yang, X. & Han, L. Toward long-term stable and highly efficient perovskite solar cells via effective charge transporting materials. *Adv. Energy Mater.* **8**, 1–25 (2018).

28. Tress, W. *et al.* The role of the hole-transport layer in perovskite solar cells - Reducing recombination and increasing absorption. in *2014 IEEE 40th Photovoltaic Specialist Conference, PVSC 2014* 1563–1566 (2014). doi:10.1109/PVSC.2014.6925216.

29. Kung, P. K. *et al.* A review of inorganic hole transport materials for perovskite

solar cells. *Adv. Mater. Interfaces* **5**, 1–35 (2018).

30. Chueh, C. C., Li, C. Z. & Jen, A. K. Y. Recent progress and perspective in solution-processed interfacial materials for efficient and stable polymer and organometal perovskite solar cells. *Energy Environ. Sci.* **8**, 1160–1189 (2015).

31. Jeong, S. H. *et al.* Characterizing the efficiency of perovskite solar cells and light-emitting diodes. *Joule* **4**, 1206–1235 (2020).

32. Lindholm, F. A., Fossum, J. G. & Burgess, E. L. Application of the superposition principle to solar-cell analysis. *IEEE Trans. Electron Devices* **26**, 165–171 (1979).

33. Inamuddin, Ahamed, M. I., Boddula, R. & Rezakazemi, M. *Fundamentals of solar cell design*. *Scrivener Publishing* (2021). doi:10.1002/9781119725022.

34. Hossain, E. & Petrovic, S. *Renewable energy crash course*. (Springer International Publishing, 2021). doi:10.1007/978-3-030-70049-2.

35. Bisquert, J. *The physics of solar cells : perovskites, organics, and photovoltaic fundamentals*. vol. 50 (CRC Press, 2017).

36. Shockley, W. & Queisser, H. J. Detailed balance limit of efficiency of p-n junction solar cells. *J. Appl. Phys.* **32**, 510–519 (1961).

37. Sha, W. E. I., Ren, X., Chen, L. & Choy, W. C. H. The efficiency limit of CH3NH3PbI3 perovskite solar cells. *Appl. Phys. Lett.* **106**, (2015).

38. Grancini, G. *et al.* One-year stable perovskite solar cells by 2D/3D interface engineering. *Nat. Commun.* **8**, 1–8 (2017).

39. Reese, M. O. *et al.* Consensus stability testing protocols for organic photovoltaic materials and devices. *Sol. Energy Mater. Sol. Cells* **95**, 1253–1267 (2011).

40. Osterwald, C. R. & McMahon, T. J. History of accelerated and qualification testing of terrestrial photovoltaic modules: A literature review. *Prog. Photovoltaics Res. Appl.* **17**, 11–33 (2009).

41. Frost, J. M. *et al.* Atomistic origins of high-performance in hybrid halide perovskite solar cells. *Nano Lett.* **14**, 2584–2590 (2014).

42. Asghar, M. I., Zhang, J., Wang, H. & Lund, P. D. Device stability of perovskite solar cells – A review. *Renew. Sustain. Energy Rev.* **77**, 131–146 (2017).

43. Duan, L. & Uddin, A. Defects and stability of perovskite solar cells: A critical analysis. *Mater. Chem. Front.* **6**, 400–417 (2022).

44. Mazumdar, S., Zhao, Y. & Zhang, X. Stability of perovskite solar cells: degradation mechanisms and remedies. *Front. Electron.* **2**, 1–34 (2021).

45. Deretzis, I. *et al.* Stability and degradation in hybrid perovskites: Is the glass half-empty or half-full? *J. Phys. Chem. Lett.* **9**, 3000–3007 (2018).

46. Misra, R. K. *et al.* Temperature- and component-dependent degradation of perovskite photovoltaic materials under concentrated sunlight. *J. Phys. Chem. Lett.* **6**, 326–330 (2015).

47. Ansari, M. I. H., Qurashi, A. & Nazeeruddin, M. K. Frontiers, opportunities, and challenges in perovskite solar cells: A critical review. *J. Photochem. Photobiol. C Photochem. Rev.* **35**, 1–24 (2018).

48. Li, C. *et al.* Iodine migration and its effect on hysteresis in perovskite solar cells. *Adv. Mater.* **28**, 2446–2454 (2016).

49. Snaith, H. J. *et al.* Anomalous hysteresis in perovskite solar cells. *J. Phys. Chem. Lett.* **5**, 1511–1515 (2014).

50. Wu, F., Pathak, R. & Qiao, Q. Origin and alleviation of J-V hysteresis in perovskite solar cells: A short review. *Catal. Today* **374**, 86–101 (2021).

51. Chen, B., Yang, M., Priya, S. & Zhu, K. Origin of J-V hysteresis in perovskite solar cells. *J. Phys. Chem. Lett.* **7**, 905–917 (2016).

52. Zhao, Y., Zhou, W., Han, Z., Yu, D. & Zhao, Q. Effects of ion migration and improvement strategies for the operational stability of perovskite solar cells. *Phys. Chem. Chem. Phys.* **23**, 94–106 (2021).

53. Calado, P. *et al.* Evidence for ion migration in hybrid perovskite solar cells with minimal hysteresis. *Nat. Commun.* **7**, 1–10 (2016).

54. Habisreutinger, S. N., Noel, N. K. & Snaith, H. J. Hysteresis index: A figure without merit for quantifying hysteresis in perovskite solar cells. *ACS Energy Lett.* **3**, 2472–2476 (2018).

55. Liu, P., Wang, W., Liu, S., Yang, H. & Shao, Z. Fundamental understanding of photocurrent hysteresis in perovskite solar cells. *Adv. Energy Mater.* **9**, 1803017 (2019).

56. Pan, H., Shao, H., Zhang, X. L., Shen, Y. & Wang, M. Interface engineering for high-efficiency perovskite solar cells. *J. Appl. Phys.* **129**, 130904 (2021).

57. Kim, J. Y., Lee, J. W., Jung, H. S., Shin, H. & Park, N. G. High-efficiency perovskite solar cells. *Chem. Rev.* **120**, 7867–7918 (2020).

58. Chen, P., Bai, Y. & Wang, L. Minimizing voltage losses in perovskite solar cells. *Small Struct.* **2**, 2000050 (2021).

59. Sarritzu, V. *et al.* Optical determination of Shockley-Read-Hall and interface recombination currents in hybrid perovskites. *Sci. Rep.* **7**, 44629 (2017).

60. Chen, Y. & Zhou, H. Defects chemistry in high-efficiency and stable perovskite solar cells. *J. Appl. Phys.* **128**, 060903 (2020).

61. Luo, D., Su, R., Zhang, W., Gong, Q. & Zhu, R. Minimizing non-radiative recombination losses in perovskite solar cells. *Nat. Rev. Mater.* **5**, 44–60 (2020).

62. Lu, H., Krishna, A., Zakeeruddin, S. M., Grätzel, M. & Hagfeldt, A. Compositional and interface engineering of organic-inorganic lead halide perovskite solar cells. *iScience* **23**, 101359 (2020).

63. Park, N. Research direction toward scalable, stable, and high efficiency perovskite solar cells. *Adv. Energy Mater.* **10**, 1903106 (2020).

64. Noel, N. K. *et al.* Enhanced photoluminescence and solar cell performance via lewis base passivation of organic–inorganic lead halide perovskites. *ACS Nano* **8**, 9815–9821 (2014).

65. Bi, E. *et al.* Diffusion engineering of ions and charge carriers for stable efficient perovskite solar cells. *Nat. Commun.* **8**, 15330 (2017).

66. Zhao, T., Chueh, C.-C., Chen, Q., Rajagopal, A. & Jen, A. K. Y. Defect passivation of organic–inorganic hybrid perovskites by diammonium iodide toward high-performance photovoltaic devices. *ACS Energy Lett.* **1**, 757–763 (2016).

67. Yu, W. *et al.* Recent advances on interface engineering of perovskite solar cells. *Nano Res.* **15**, 85–103 (2022).

68. Shao, Y., Xiao, Z., Bi, C., Yuan, Y. & Huang, J. Origin and elimination of photocurrent hysteresis by fullerene passivation in CH3NH3PbI3 planar heterojunction solar cells. *Nat. Commun.* **5**, 5784 (2014).

69. Abate, A. *et al.* Supramolecular halogen bond passivation of organic-inorganic halide perovskite solar cells. *Nano Lett.* **14**, 3247–3254 (2014).

70. Song, D. *et al.* Dual function interfacial layer for highly efficient and stable lead halide perovskite solar cells. *J. Mater. Chem. A* **4**, 6091–6097 (2016).

71. Yang, Z. *et al.* Multifunctional phosphorus-containing lewis acid and base passivation enabling efficient and moisture-stable perovskite solar cells. *Adv. Funct. Mater.* **30**, 1910710 (2020).

72. Chaudhary, B. *et al.* Poly(4-vinylpyridine)-based interfacial passivation to enhance voltage and moisture stability of lead halide perovskite solar cells. *ChemSusChem* **10**, 2473–2479 (2017).

73. Wen, T. Y. *et al.* Surface electronic modification of perovskite thin film with water-resistant electron delocalized molecules for stable and efficient photovoltaics. *Adv. Energy Mater.* **8**, 1703143 (2018).

74. Zeng, Q. *et al.* Polymer-passivated inorganic cesium lead mixed-halide perovskites for stable and efficient solar cells with high open-circuit voltage over 1.3 V. *Adv. Mater.* **30**, 1705393 (2018).

75. Lin, Y. *et al.* π-conjugated lewis base: Efficient trap-passivation and charge-extraction for hybrid perovskite solar cells. *Adv. Mater.* **29**, 1604545 (2017).

76. Zhang, H. *et al.* Efficient and stable chemical passivation on perovskite surface via bidentate anchoring. *Adv. Energy Mater.* **9**, 1803573 (2019).

77. Liu, L. *et al.* Grain-boundary "patches" by in situ conversion to enhance perovskite solar cells stability. *Adv. Mater.* **30**, 1800544 (2018).

78. Bi, D. *et al.* Multifunctional molecular modulators for perovskite solar cells with over 20% efficiency and high operational stability. *Nat. Commun.* **9**, 4482 (2018).

79. Yang, S. *et al.* Stabilizing halide perovskite surfaces for solar cell operation with wide-bandgap lead oxysalts. *Science (80-.).* **365**, 473–478 (2019).

80. Godding, J. S. W. *et al.* Oxidative passivation of metal halide perovskites. *Joule* **3**, 2716–2731 (2019).

81. Huang, X., Guo, H., Wang, K. & Liu, X. Ionic liquid induced surface trap-state passivation for efficient perovskite hybrid solar cells. *Org. Electron.* **41**, 42–48 (2017).

82. Zu, F. *et al.* Surface state density determines the energy level alignment at hybrid perovskite/electron acceptors interfaces. *ACS Appl. Mater. Interfaces* **9**, 41546–41552 (2017).

83. Fu, L. *et al.* Defect passivation strategies in perovskites for an enhanced photovoltaic performance. *Energy Environ. Sci.* **13**, 4017–4056 (2020).

84. Jung, M., Shin, T. J., Seo, J., Kim, G. & Seok, S. Il. Structural features and their functions in surfactant-armoured methylammonium lead iodide perovskites for highly efficient and stable solar cells. *Energy Environ. Sci.* **11**, 2188–2197 (2018).

85. Alharbi, E. A. *et al.* Atomic-level passivation mechanism of ammonium salts enabling highly efficient perovskite solar cells. *Nat. Commun.* **10**, 3008 (2019).

86. Jiang, X. *et al.* Deeper insight into the role of organic ammonium cations in reducing surface defects of the perovskite film. *Angew. Chemie Int. Ed.* **61**, (2022).

87. Jiang, Q. *et al.* Surface passivation of perovskite film for efficient solar cells. *Nat. Photonics* **13**, 460–466 (2019).

88. Zhu, H. *et al.* Tailored amphiphilic molecular mitigators for stable perovskite solar cells with 23.5% efficiency. *Adv. Mater.* **32**, 1907757 (2020).

89. Gunes, U. *et al.* A thienothiophene-based cation treatment allows semitransparent perovskite solar cells with improved efficiency and stability.

Adv. Funct. Mater. **31**, 2103130 (2021).

90. Liu, C. *et al.* Tuning structural isomers of phenylenediammonium to afford efficient and stable perovskite solar cells and modules. *Nat. Commun.* **12**, 6394 (2021).

91. Hu, Y. *et al.* Hybrid perovskite/perovskite heterojunction solar cells. *ACS Nano* **10**, 5999–6007 (2016).

92. Wang, F. *et al.* Phenylalkylamine passivation of organolead halide perovskites enabling high-efficiency and air-stable photovoltaic cells. *Adv. Mater.* **28**, 9986–9992 (2016).

93. Zhao, B. *et al.* Introduction of multifunctional triphenylamino derivatives at the perovskite/HTL interface to promote efficiency and stability of perovskite solar cells. *ACS Appl. Mater. Interfaces* **12**, 9300–9306 (2020).

94. Abate, S. Y. *et al.* Universal surface passivation of organic–inorganic halide perovskite films by tetraoctylammonium chloride for high-performance and stable perovskite solar cells. *ACS Appl. Mater. Interfaces* **14**, 28044–28059 (2022).

95. Chu, Z. *et al.* Emerging low-dimensional crystal structure of metal halide perovskite optoelectronic materials and devices. *Small Struct.* **2**, 2000133 (2021).

96. Zhang, F. *et al.* Advances in two-dimensional organic–inorganic hybrid perovskites. *Energy Environ. Sci.* **13**, 1154–1186 (2020).

97. Zhou, M., Fei, C., Sarmiento, J. S. & Wang, H. Manipulating the phase distributions and carrier transfers in hybrid quasi-two-dimensional perovskite films. *Sol. RRL* **3**, 1800359 (2019).

98. Ortiz-Cervantes, C., Carmona-Monroy, P. & Solis-Ibarra, D. Two-dimensional halide perovskites in solar cells: 2D or not 2D? *ChemSusChem* **12**, 1560–1575 (2019).

99. Liu, C., Cheng, Y.-B. & Ge, Z. Understanding of perovskite crystal growth and film formation in scalable deposition processes. *Chem. Soc. Rev.* **49**, 1653–1687 (2020).

100. Liu, P. *et al.* High-quality Ruddlesden–Popper perovskite film formation for high-performance perovskite solar cells. *Adv. Mater.* **33**, 2002582 (2021).

101. Krishna, A., Gottis, S., Nazeeruddin, M. K. & Sauvage, F. Mixed dimensional 2D/3D hybrid perovskite absorbers: The future of perovskite solar cells? *Adv. Funct. Mater.* **29**, 1806482 (2018).

102. Akin, S. *et al.* Organic ammonium halide modulators as effective strategy for enhanced perovskite photovoltaic performance. *Adv. Sci.* **8**, 2004593 (2021).

103. Smith, I. C., Hoke, E. T., Solis-Ibarra, D., McGehee, M. D. & Karunadasa, H. I. A Layered Hybrid Perovskite Solar-Cell Absorber with Enhanced Moisture Stability. *Angew. Chemie Int. Ed.* **53**, 11232–11235 (2014).

104. Koh, T. M. *et al.* Enhancing moisture tolerance in efficient hybrid 3D/2D perovskite photovoltaics. *J. Mater. Chem. A* **6**, 2122–2128 (2018).

105. Kim, H. *et al.* Optimal interfacial engineering with different length of alkylammonium halide for efficient and stable perovskite solar cells. *Adv. Energy Mater.* **9**, 1902740 (2019).

106. Yoo, H.-S. & Park, N.-G. Post-treatment of perovskite film with phenylalkylammonium iodide for hysteresis-less perovskite solar cells. *Sol. Energy Mater. Sol. Cells* **179**, 57–65 (2018).

107. Ghoreishi, F. S. *et al.* Enhanced performance of CH3NH3PbI3 perovskite solar cells via interface modification using phenyl ammonium iodide derivatives. *J. Power Sources* **473**, 228492 (2020).

108. Fu, W. *et al.* Tailoring the functionality of organic spacer cations for efficient and stable quasi-2D perovskite solar cells. *Adv. Funct. Mater.* **29**, 1900221 (2019).

109. Zhou, Q. *et al.* Fluoroaromatic cation-assisted planar junction perovskite solar cells with improved VOC and stability: The role of fluorination position. *Sol. RRL* **4**, 2000107 (2020).

110. Zhuang, J. *et al.* Interfacial passivation for perovskite solar cells: The effects of the functional group in phenethylammonium iodide. *ACS Energy Lett.* **4**, 2913–2921 (2019).

111. Meng, F., Shang, X., Gao, D., Zhang, W. & Chen, C. Functionalizing phenethylammonium by methoxy to achieve low-dimensional interface defects passivation for efficient and stable perovskite solar cells. *Nanotechnology* **33**, 065201 (2022).

112. Lin, Y. *et al.* Enhanced thermal stability in perovskite solar cells by assembling 2D/3D stacking structures. *J. Phys. Chem. Lett.* **9**, 654–658 (2018).

113. Kim, H. *et al.* Self-crystallized multifunctional 2D perovskite for efficient and stable perovskite solar cells. *Adv. Funct. Mater.* **30**, 1910620 (2020).

114. Liang, L., Luo, H., Hu, J., Li, H. & Gao, P. Efficient perovskite solar cells by reducing interface-mediated recombination: A bulky amine approach. *Adv. Energy Mater.* **10**, 2000197 (2020).

115. Xia, J. *et al.* Deep surface passivation for efficient and hydrophobic perovskite solar cells. *J. Mater. Chem. A* **9**, 2919–2927 (2021).

116. Ananda, W. External quantum efficiency measurement of solar cell. in *2017*

15th International Conference on Quality in Research (QiR) : International Symposium on Electrical and Computer Engineering vols 2017-Decem 450–456 (IEEE, 2017).

117. Pazoki, M., Hagfeldt, A. & Edvinsson, T. *Characterization techniques for perovskite solar cell materials*. *Characterization Techniques for Perovskite Solar Cell Materials* (Elsevier, 2019). doi:10.1016/C2017-0-01993-6.

118. Saliba, M. & Etgar, L. Current density mismatch in perovskite solar cells. *ACS Energy Lett.* **5**, 2886–2888 (2020).

119. Peng *et al.* High-quality perovskite CH3NH3PbI3 thin films for solar cells prepared by single-source thermal evaporation combined with solvent treatment. *Materials (Basel).* **12**, 1237 (2019).

120. Zatsepin, D. A. & Zatsepin, A. F. Ultraviolet photoelectron spectroscopy – materials science technique. in *Spectroscopy for Materials Characterization* 383–403 (John Wiley & Sons, Inc, 2021). doi:10.1002/9781119698029.ch13.

121. Li, Y. *et al.* Bifunctional organic spacers for formamidinium-based hybrid Dion–Jacobson two-dimensional perovskite solar cells. *Nano Lett.* **19**, 150–157 (2019).

122. Fujiwara, H. *et al.* Analysis of optical and recombination losses in solar cells. in *Spectroscopic Ellipsometry for Photovoltaics. Springer Series in Optical Sciences* vol. 214 29–82 (Springer, Cham, 2018).

123. Prasanna, R. *et al.* Band gap tuning via lattice contraction and octahedral tilting in perovskite materials for photovoltaics. *J. Am. Chem. Soc.* **139**, 11117–11124 (2017).

124. Bou, A. *et al.* Beyond impedance spectroscopy of perovskite solar cells: Insights from the spectral correlation of the electrooptical frequency techniques. *J. Phys. Chem. Lett.* **11**, 8654–8659 (2020).

125. Long, Y. *et al.* Crossover from itinerant-electron to localized-electron behavior in Sr1− xCaxCrO3 perovskite solid solution. *J. Phys. Condens. Matter* **23**, 355601 (2011).

126. Xue, J., Wang, R. & Yang, Y. The surface of halide perovskites from nano to bulk. *Nat. Rev. Mater.* **5**, 809–827 (2020).

127. Zhang, Y. *et al.* Water-repellent perovskites induced by a blend of organic halide salts for efficient and stable solar cells. *ACS Appl. Mater. Interfaces* **13**, 33172–33181 (2021).